

## Review Article

# Optical Response Near the Soft X-Ray Absorption Edges and Structural Studies of Low Optical Contrast System Using Soft X-Ray Resonant Reflectivity

**Maheswar Nayak and Gyanendra S. Lodha**

*X-Ray Optics Section, Indus Synchrotrons Utilization Division, Raja Ramanna Centre for Advanced Technology, Indore 452013, India*

Correspondence should be addressed to Maheswar Nayak, mnayak@rrcat.gov.in and Gyanendra S. Lodha, lodha@rrcat.gov.in

Received 11 October 2010; Revised 10 January 2011; Accepted 7 February 2011

Academic Editor: Derrick S. F. Crothers

Copyright © 2011 M. Nayak and G. S. Lodha. This is an open access article distributed under the Creative Commons Attribution License, which permits unrestricted use, distribution, and reproduction in any medium, provided the original work is properly cited.

Fine structure features of energy-dependent atomic scattering factor near the atomic absorption edge, are used for structural analysis of low-Z containing thin film structures. The scattering contrast undergoes large and abrupt change as the incident photon energy approaches the natural frequency of the atom and is sensitive to variation in atomic composition and atomic density. Soft X-ray resonant reflectivity is utilized for determination of composition at the buried interfaces with subnanometer sensitivity. This is demonstrated through characterization of Mo/Si multilayers near Si L-edge. We also demonstrate the possibility of probing variation of atomic density in thin films, through the characterization of Fe/B<sub>4</sub>C structure, near B K-edge. Sensitivity of soft X-ray resonant reflectivity to native oxide is demonstrated through characterization of BN films near B K-edge.

## 1. Introduction

Hard X-ray reflectivity (XRR) probes electron density profile (EDP) and is an important nondestructive research tool to probe interfaces in thin film multilayer structure [1]. The large dynamic range and high momentum scattering vector range of XRR (incident X-ray energy is far away from absorption edge) allow determination of structural parameters such as thickness, roughness, density, and interface interdiffusion profile in thin film structures with high electron density contrast. XRR determines electron density of a layer. Using XRR measurements it is difficult to extract the layer composition from the electron density for following conditions: (i) layers in a multilayer containing an unknown amount of impurity, usually incorporated during film deposition, (ii) layers contain several components (e.g., C impurity in a Si layer) with nearly equal electron density, (iii) formation of low electron density contrast compound at the buried interfaces, (iv) formation of native oxide and change in compositions of oxide, with poor electron density contrast, (v) significant change in porosity of a layer. For example, in a Pt/C multilayer, even a 15% change in

the electron density of the C-layers does not produce a significant change in XRR [2]. In high reflectivity X-ray multilayer structures, where strong standing wave fields are generated near the Bragg angle, XRR is combined with X-ray standing wave (XSW) to address this problem. Fluorescence from different elements in the multilayer is simultaneously measured along with the reflectivity. Combined XSW-XRR can determine interface roughness and layer composition. Composition can be determined [3] with a precision of ~2% with depth resolution of ~0.1 nm [2]. The adaption of this combination is difficult for thin films and multilayer structure which are not periodic. Further, for low Z/low Z system, the standing wave fields are weak, followed by low fluorescent yield for low Z elements.

In XRR, only intensity is measured and the phase information is lost. Real space information is obtained by modeling of EDP. The reflectivity profile is calculated by recursion relation [1] taking different layers with constant electron densities [4]. The calculated XRR profile is least square fitted with the measured profile by varying large number of parameters such as film thickness, optical constants, and roughness. This works well if the initial guess of EDP is

close to the actual EDP of the structure. Extracting the real parameters became difficult for low density contrast system where the amplitude modulation of oscillations is very small. Sanyal et al. [5] have proposed box refining method based on Distorted Wave Born Approximation formalism [6] to determine small fluctuation in EDP of Langmuir Blodgett films. The low electron density contrast problem is also addressed using one-dimensional Patterson function (the Fourier transform (FT)) of normalized reflectivity [7–16]. The maxima in FT give location of layer thickness, which helps in reducing the number of free parameters during least square fitting. In case of small variation in electron density, it is difficult to identify modulation in the XRR patterns while FT generates secondary maxima, indicating layer formation. Yu et al. [9] have observed internal layering in thin film ( $\sim 4.5$ – $9$  nm) liquid film using XRR. Secondary maxima in Patterson function indicated layer formation near the solid-liquid interface with a period of  $\sim 1$  nm. Seeck et al. [10] have demonstrated that interfacial parameters can be determined in polymers, where the difference in the electron density is small. By simulation they have shown that, although there is no significant change in specular reflectivity pattern with  $\sim 5\%$  contrast, FT of specular reflectivity data indicates the sensitivity through the secondary maxima in FT. They have also shown by simulation, the effect of different roughness and lower limit in  $z$ -component of momentum transfer vector on the FT profile. The limitation of this technique is that only thickness of the film can be known from position of maxima in FT. Others parameters need to be obtained from modeling of EDP which are not unique and impose difficulty in case of low contrast system and technique is not sensitive to variation in atomic composition. An alternate way of finding optical contrast is measuring reflectivity by tuning incident photon energy near the atomic absorption edge of the constituent element of the thin film multilayer system, which we investigate in this paper.

X-ray scattering shows a resonant behavior when the X-ray energy is tuned near the atomic absorption edges of an element in a material. The resonant effect originates mostly from tightly bound inner electrons, with strong variation of the atomic scattering factor near the edges [17, 18]. Electronic transition and hence atomic scattering factor of probed elements get modified due to local chemical environment. X-ray resonant scattering combines spectroscopy with the scattering techniques. Vettier [19] has presented three main properties of X-ray resonance: the large enhancement of scattering amplitude, the chemical selectivity and the sensitivity to the symmetry of electronic levels. Using resonant scattering principle, the spectroscopic nature of the electronic transitions of probed elements and their modifications due to local chemical environment can be studied using polarized nature of synchrotron radiation beam available from insertion device-based synchrotron source [20]. The strong variation of atomic scattering factors and hence optical constants provide an opportunity in getting high and tunable optical contrast [21]. The use of X-ray techniques based on resonant scattering phenomena has been increasing ever since continuously tunable monochromatic X-rays became available at synchrotron

sources. While the imaginary part of the scattering factor has been used widely in the X-ray absorption fine structure spectroscopy and related techniques [22] more attention has recently been paid towards the use of the real part of the scattering factor. In the hard X-ray region, resonant X-ray scattering/reflectivity is utilized as tool in many different fields, for examples to study ion distribution at biomembranes [23], spectroscopic structures of ion adsorbed at oxide-water interfaces [24], chemical depth profile of passive oxide [25], magnetic material [26], and monolayer of bromostearic acid at the air/water interface [27], charged aqueous surfaces/interfaces [28], metal oxides thin films [29]. Sanyal et al. have proposed a model-independent method to obtain density profile by inverting reflectivity profile using anomalous XRR [30]. They have demonstrated this on organic thin films by tuning photon energies close to, and away from, absorption edge of substrate (germanium). Using the above method, Ohkawa et al. [31] have determined the structure of Al/C multilayers deposited on germanium by measuring reflectivity at two different photon energies near germanium K-absorption edge. Park and Fenter [32] have proposed a model-independent formalism for determination of element-specific partial structure at buried interfaces using phase-dependent behavior in reflectivity at a fixed momentum transfer near the absorption edge. They have demonstrated this method for studying ion distribution muscovite (001) aqueous solution interfaces. Feynson et al. [33] have studied interface morphology of epitaxially grown Fe/Cr/Fe using anomalous X-ray scattering/reflectivity near Cr K-absorption edge. Using contrast variation in resonant X-ray scattering, they have quantitatively extracted structure of samples, including buried layers and top oxide layer.

In hard X-ray region, Straginer et al. [34] have proposed diffraction anomalous fine structure (DAFS), which combines long-range order sensitivity of diffraction techniques with the short-range order sensitivity of absorption techniques. They demonstrated that, absorption-like information can be obtained from scattering measurements. Since real and imaginary part of atomic scattering factors are related causality, so the energy-dependent X-ray diffraction at fixed momentum transfer can be used to provide the short-range local atomic order information generally obtained from X-ray absorption measurements. In the extended fine structure region, DAFS provides short-range structural information such as the bond lengths, the neighbor types, and the coordination numbers for the atoms surrounding the resonating scattering atoms. In the near-edge region, DAFS provides the same structural and spectroscopic sensitivities as X-ray absorption near edge spectroscopy. DAFS can be used to provide enhanced site and spatial sensitivities for poly-atomic and/or spatially modulated structures. Létoublon et al. [35] used DAFS for the determination of strain, size and composition of semiconducting quantum sticks. Luo et al. [36] have studied structural changes in Cu/NiFe annealed multilayers using glancing incidence X-ray reflectivity as function of incident X-ray energy under fixed scattering vector. They have demonstrated the possibility to determine the density and composition as the energy is varied through

the K-absorption of the constituent elements. Soft X-ray resonant reflectivity is a similar approach as DAFS but based on strong variation in atomic scattering factors due to electronic transitions of the probed elements and their modifications due to local chemical environment. Resonant soft X-ray reflectivity provides not only the chance for varying the scattering contrasts or excitation of standing waves but can combine X-ray reflectivity with X-ray spectroscopy.

Soft X-ray resonant reflectivity/scattering studies are finding application in soft mater polymer films [37–46], and biological samples [47]. However the utility of soft X-ray resonant for studies of atomic composition at buried interface, depth profiling of variation in atomic density, native oxide and films of nearly equal electron density studies of hard condensed matter thin films/multilayers is not significantly exploited. Hogrefe and Kunz [48] have done soft X-ray scattering study from rough gold surfaces using both experimental and model analysis. Carlisle et al. [49] have demonstrated capability of soft X-ray resonant fluorescence for probing buried monolayer of boron nitride and examined changes in electronic structure using the strong  $\pi^*$  resonance feature near the B (1s) threshold. Adamczyk et al. [50] studied PMMA coated silicon sample by tuning photon energy near C K-edge. They have attempted to distinguish the buried Si-PMMA interface from the top free surface of the PMMA by exploring element-specific resonant scattering. Hattén et al. [51] have used resonant soft X-ray diffraction near L-edge of 3d transition metal to observe changes in the intensity of allowed Bragg reflections. Using these strong resonances, they have observed the antiferromagnetic ordering of 3d spins and formation of orbital order in doped manganites. Singh et al. [52] have studied growth kinetics and compositional analysis of silicon rich a-SiN<sub>x</sub>:H films using soft X-ray resonant reflectivity near Si L-absorption edge. Wadati et al. [53] have studied interface reconstructions in SrTiO<sub>3</sub>/LaAlO<sub>3</sub> super lattices using resonant soft X-ray scattering near the Ti 2p and O 1s. By measuring reflectivity near the edge, they have observed the forbidden (003) peak in “ideal” super structure, and claimed distinct reconstructions at two interfaces by breaking the hetero structure symmetry. Earlier we had demonstrated the possibility of probing interlayer composition [54] at buried interfaces and porosity [55] using soft X-ray resonant reflectivity.

The main emphasis in this paper is to provide comprehensive information about the possibility of characterization of low contrast condensed matter thin films using soft X-ray resonant reflectivity (SXRR). We also demonstrate the capability of the SXRR to combine structural with chemical analysis. The capability of SXRR method for analysis at nanometer scale buried layer will be presented through representative applications. In Section 2, we present the background on interaction of soft X-rays with matter. This is followed by the optical response near the atomic edge. This is followed by a brief review on modeling of reflectivity from thin film and multilayers using dynamical theory, and correlation of scattering contrast to optical constants near the absorption edge. Experimental details are described in Section 3. In Section 4, we presents results on

the measured optical response near absorption edge for Si (at L-edge), B<sub>4</sub>C (at B K-edge) and BN (at B K-edge). This is followed by the representative results of the possibility to determine interlayer composition at buried interfaces. This is demonstrated through simulations and experiments on Mo/Si multilayers. After that we present the determination of depth profiling of variation in atomic density in Fe/B<sub>4</sub>C. This is followed by possibility of determining nanometer scale oxide layer in low-Z material thin film. This is demonstrated through characterization of BN thin film.

## 2. General Aspects of Soft X-Ray—Matter Interaction

**2.1. Origin of Resonant X-Ray Scattering.** To understand the capabilities of soft X-ray resonant scattering/reflectivity method and interpret resonant profile for obtaining structural and chemical information one needs to understand the way X-ray interact with matter. Although rigorous quantum mechanical calculations provide more accurate way of treating light scattering [56], much can be learned by scattering from a simple semiclassical atomic model [57, 58] and the basic results are similar in form to those derived by quantum mechanical models. In the semiclassical model, the total scattering cross section of multielectron atom is given by [58]

$$\sigma(\omega, q) = \left[ \frac{8\pi r_e^2}{3} \right] \times \left[ \sum_s \frac{g_s \omega^2 e^{-iq \cdot \Delta r_s}}{\omega^2 - \omega_s^2 + i\gamma\omega} \right]^2, \quad (1)$$

where  $r_e = 2.82 \times 10^{-15}$  m is the classical electron radius,  $e^{-iq \cdot \Delta r_s}$  is the phase factor,  $\gamma$  is the damping factor and  $q$  is the momentum transfer vector. The magnitude of momentum transfer vector is  $|q| = 2k_i \sin \theta = 4\pi \sin \theta / \lambda$ .  $g_s$  is the oscillator strength,  $\omega_s$  is the resonance frequency. In (1), the first term is the Thomson cross section, which is the scattering cross section by a free (unbound) electron. The second term inside square bracket is the atomic scattering factor. The atomic scattering factor is the effective number of electrons in an atom that takes part in the scattering process. Atomic scattering cross section of a multielectron atom is equal to Thomson scattering multiplied by square of atomic scattering factor. Frequency-dependent scattering cross section has a strong resonance near the resonance frequency of bound electron, with peak scattering cross section very large compared to the scattering by free electron. It must be noted that the expression  $q \cdot \Delta r_s$  gives the phase variation of the scattered fields, due to differing electron positions in semiclassical approximation, as seen by the observer. Neglecting the magnetic scattering terms, the frequency and momentum vector dependent complex atomic scattering factor can also be written in the form

$$f(q, \omega) = f_0(q) + \Delta f_1(\omega) - i\Delta f_2(\omega). \quad (2)$$

The nonresonant  $q$  dependent first term is due to contribution from free electrons and is proportional to the Fourier transform of atomic charge distribution. The frequency-dependent resonant terms arises due to strongly bound core

electrons. The resonant term strongly varies with incident photon frequency near the atomic absorption edge. Here please note that, in quantum mechanical approach,  $\Delta f$  depends separately on the incident and scattered photon wave vectors ( $k_i$  and  $k_r$ ) apart from photon frequency. Thus in general  $\Delta f$  is a tensor, and is not proportional to the Fourier transform of the total or subshell charge density [19]. However, it is experimentally established that  $k_i$  and  $k_r$  dependencies are often very small, and consequently the photon frequency and momenta dependent  $\Delta f(\omega, k_i, k_f)$  is generally approximated by the forward scattering limit  $\Delta f(\omega)$  [59]. The detailed expression for resonant term of atomic scattering factor is given by Vettier [19], and is an anisotropic tensors of the polarization vectors. In general, for simplicity, (2) can be written in terms of real and imaginary part as  $f(q, \omega) = f_1(q, \omega) - if_2(\omega)$  with  $f_1(q, \omega) = f_0(q) + \Delta f_1(\omega)$  and  $f_2(\omega) = \Delta f_2(\omega)$ . In soft X-ray region, when the atom is much smaller than X-ray wavelength ( $\lambda/a_0 \gg 1$ , where  $a_0$  is Bohr radius), the amplitudes scattered by the individual electrons add coherently for all values of the polar angle. On the other hand, for hard X-ray wavelengths, the coherent superposition takes place only near the forward direction ( $\theta \rightarrow 0$ ). In these special cases, the frequency and momentum vector dependent atomic scattering factor  $f(q, \omega)$  reduces to only frequency-dependent term. And can be written as

$$f^0(\omega) = f_1^0(\omega) - if_2^0(\omega). \quad (3)$$

Here in our present study of soft X-ray and extreme ultra violet radiation scattering by low- $Z$  atoms,  $f(q, \omega) \rightarrow f^0(\omega) \rightarrow \sum_s g_s = Z$ , where  $Z$  is atomic number. Then (1) reduces to  $\sigma(\omega) \cong \sigma_T Z^2$ . For example, let us calculate the scattering of a soft X-ray radiation at 1.24 keV ( $\sim 10 \text{ \AA}$ ) by a boron atom ( $Z = 5$ ). This energy is well above the binding energy of K-shell electron of boron ( $\sim 188 \text{ eV}$ ) and incident wavelength is much greater than the Bohr radius,  $a_0$ . Hence boron atom scatters  $\sim 25$  times more than that of Thomson scattering value. Scattered electric field by each of these five electrons of boron, add in-phase at all distant observation points. That means all five electrons scatter radiation coherently in all the direction. The resonant effect originates mostly from tightly bound inner electrons. If the incident photon frequency  $\omega$  is in the vicinity of an atomic resonance, the response of the corresponding core electrons is influenced by their binding to the nucleus. The photon generates real and virtual transitions in which it is absorbed and reemitted. This is the origin of resonance terms in the expression for scattering rates.

In the condensed material phase, the atomic scattering factor can be further subdivided into smooth, bare atom contribution,  $f^0(\omega) = f_1^0(\omega) - if_2^0(\omega)$ , and oscillating DAFS contribution,  $f_2^0(\omega)\chi(\omega)$  with  $\chi = \chi_1 + i\chi_2$ . The bare atom contribution is the same as that for isolated single atom X-ray scattering whereas oscillating DAFS contribution is produced by the neighboring atoms and provides the local structure information for condensed phase atoms. This separation of  $f^0(\omega) = [f_1^0(\omega) - if_2^0(\omega)] + [f_2^0(\omega)\chi(\omega)]$  into atomic and fine-structure components is analogous to the usual X-ray

absorption fine structure separation and has been discussed more detailed by Stragier et al. [34] to combine long-range order sensitivity of diffraction techniques with the short-range order sensitivity of absorption techniques.

**2.2. Physical Picture of the Resonant Scattering Factor.** Far from the absorption edge, electron with binding energy less than incident photon energy scatter according to Thomson free electron model [58] and phase of polarization lags by  $180^\circ$  to the applied field. Bound electrons with energy greater than incident photon energy, contribute to in-phase polarization. This contribution is negligible compared to Thomson free electron scattering. Near the absorption edge, the in-phase polarization component becomes significant due to quantum mechanical exchange of oscillator strengths between various core levels, and this contribution cannot be neglected [59]. The approximation fails badly below the plasma frequency ( $= \sqrt{4\pi N_e r_0 c^2}$ , where  $N_e$  is the density of free electrons) of valence or conduction electrons and gives a strong, broad absorption. In this region Rayleigh, that is, resonant scattering must be taken into account. At the energy just below the atomic absorption edge, electron undergoes virtual transition in modified electric field of the atom. The electron is not able to move out of the local environment of the atom and contributes to in-phase polarization with incident field of the photon. However, just above the absorption edge energy, the electron moves out of the local environment of the atom, leading to real transition of the electron. In case, the in-plane polarization component is sufficient to overcome the out of phase polarization component, real part of atomic scattering factor  $f_1^0$  undergoes sign reversal.

Benfatto and Felici [60] have given a detailed theory of the resonant atomic scattering factor, based on a multiple-scattering approach. Henke et al. [61] have given a comprehensive tabulation of values for the atomic scattering factor calculated for all the elements  $Z = 1 - 92$  in the energy range 50 eV to 30 keV, and measured values for some elements. The absorption (imaginary) part of atomic scattering factor is from transmission measurements and dispersion (real) part is determined using the Kramers-Kronig relation. At the absorption edges, uncertainties in their tabulated values are large, due to the missing oscillator strength in the absorption coefficient data used. The real part of the atomic scattering factor  $f_1^0$  can be calculated from  $f_2^0$  by the Kramer's-Kronig integral transformation given by [62]

$$f_1^0(E_1) = \frac{2}{\pi} P \int_0^{+\infty} \left[ \frac{E f_2^0(E)}{E^2 - E_1^2} \right] dE. \quad (4)$$

Conditions favorable for a sign change in the X-ray scattering factor include a strong absorption edge with a sharp onset, to provide an in-phase "bound-electron" polarization comparable to the out-of-phase "free-electron" contribution. These conditions do not favor edges originating from levels with only a few electrons, especially s-like levels with just two electrons, such as K, L<sub>I</sub>, M<sub>I</sub>, and so forth, edges except K-edges in the second-period elements, which lack well-developed L shell. More likely are elements



with  $L_{II, III}$ ,  $M_{IV, V}$ , and so forth, edges, which involve a large number of electrons. Secondly, the edge in question must be sufficiently isolated, so that the high-energy absorption tails of transitions at lower energy is small at the edge. Otherwise, the jump ratio at the edge will not be large, and the edge not sufficiently abrupt to give strong anomalous dispersion. Further, absorptions at lower energies must have sufficiently low total oscillator strength, so that out-of-phase polarization component does not overwhelm the in-phase component due to the “bound-electron” transitions. These requirements do not favor the 3d transition metals, in which a strong, broad M-shell absorption extends in the vacuum ultra-violet region. The above considerations suggest that the  $L_{II, III}$  edges of the third-period elements such as Al, Si, and P, are among the most favorable candidates for sign reversal of  $f_1^0$ . Other possibilities include isolated  $M_{IV, V}$  edges in the fourth-period elements and K-edges in the second period elements.

Figure 1 shows the variation of  $f_1^0$  and  $f_2^0$  (super script zero is for either long wavelength limit or for forward scattering,  $\theta \ll 1$ ) as function of photon energy (for Si using the Henke et al. [61] atomic scattering database). The real part  $f_1^0$  approaches a value equal to the atomic number  $Z$  (number of electrons per atom) for the higher photon energies except at the absorption edges. This is because, at higher energies, all the electrons behave as free electrons. For perfectly free electron all the energy received by the electron is reradiated. Losses are introduced in the imaginary part  $f_2^0$ . The imaginary part  $f_2^0$  decreases in general, but increases at the absorption edge. Close to the absorption edge,  $f_1^0$  and  $f_2^0$  vary rapidly with energy (resonance effect). There is a sharp jump in  $f_2^0$  from below the edge (in energy), while  $f_1^0$  dips significantly through the edge. Since the atomic-like assumption is clearly a poor approximation in the vicinity of absorption edges because of chemical environment, the resolution of the calculations of Henke et al. is not sufficient to establish the details of the dispersion at the edges. Sign change in  $f_1^0$  would have several intriguing consequences. For example, in such “anomalous” regions the intensity of the forward scattering, which is proportional to  $(f_1^0)^2 + (f_2^0)^2$ , exhibits a sharp tunable contrast variation. The other two important properties of X-ray resonant scattering are the chemical selectivity and the sensitivity to the electronic shells [19]. The atomic scattering factor of a compound can be calculated using the scattering factor of individual atoms weighted with density [63]. At the absorption edges, fine structure features of the atomic scattering factors depend on the chemical environment of an atom. At the absorption edges,  $f_1^0$  and  $f_2^0$  can vary drastically with a small change in the composition of the materials and hence would make possible analysis of composition of buried interfaces, variation of atomic density in thin film and structural parameters of low optical contrast structure. The interaction at resonant energies is a fingerprint of chemical elements and the valence state. Thus it is possible selectively tune the photon energy to a given absorption edge, and to enhance the response from a given element (or a valence state of this particular element) in an alloy or compound.

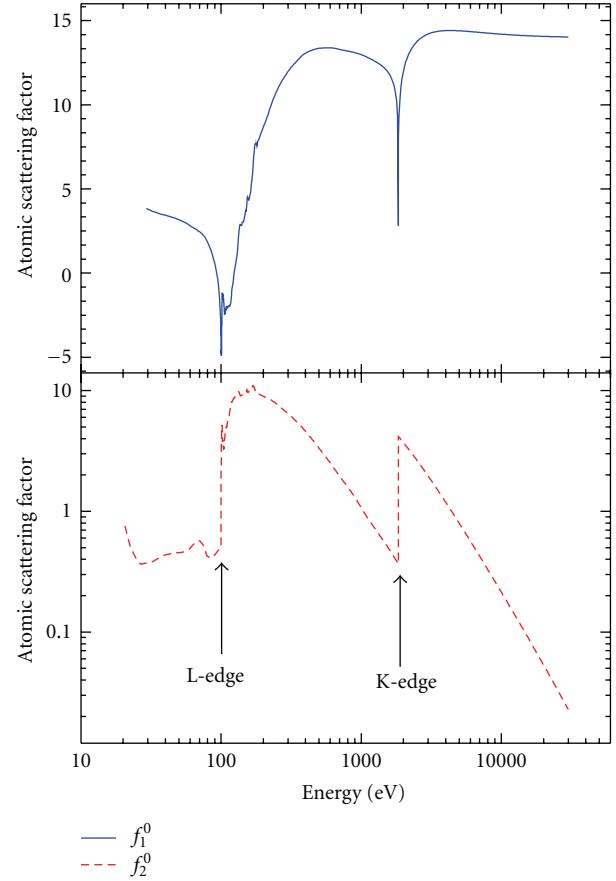


FIGURE 1: Real  $f_1^0$  and imaginary  $f_2^0$  part of the atomic scattering factor of Si as a function of photon energy.

**2.3. Optical Properties of Materials.** The interaction of X-rays with matter can also be described through the optical properties of materials using refractive index. Since the scattering process involves both elastic and inelastic (dissipative) processes, the frequency-dependent refractive index is in general a complex quantity in the form  $n(\omega) = 1 - \delta(\omega) + i\beta(\omega)$ , where  $\delta$  is the dispersion term and  $\beta$  is the absorption term. These terms are known as optical constants and are related to the real and imaginary part of the atomic scattering factor as  $(\delta + i\beta) = \chi(f_1^0 + if_2^0)$ , where  $\chi = N_a r_e \lambda^2 / 2\pi$  with  $N_a$  is the number of atoms per unit volume. The corresponding atomic photo absorption cross section is given by  $\sigma_{\text{abs}}(\omega) = 2r_e \lambda f_2^0(\omega)$ . Generally, the real part of the complex energy-dependent refractive index is less than unity for energies above the valence-electron plasma frequency (commonly 10–20 eV), so X-ray is totally externally reflected at the material/air or vacuum interface below the critical angle  $\theta_c \approx \sqrt{2\delta}$ . As discussed in Section 2.2, for some cases the real part of refractive index  $(1 - \delta)$  exceeds unity near some X-ray absorption edge because of  $f_1^0(\omega)$  becoming negative. In such an “anomalous” region, total external reflection does not occur at any angle. In the hard X-ray to vacuum ultraviolet region, the optical constants are generally measured using angle-dependent reflectivity measurements [64–67] (also see ref. [54, 55], refraction correction in diffraction from a

multilayer [68–70] and transmission measurements [61]. In the transmission measurements,  $\beta$  is measured and  $\delta$  is obtained using the Kramers-Kronig relation whereas, in reflectivity measurements, both  $\delta$  and  $\beta$  are obtained from a fitting of the Fresnel equations to the reflectivity data. The other techniques which can also be used for optical constant measurements at longer wavelengths are ellipsometry [71], electron energy loss spectrometry [72] and interferometry [73].

As we discussed in Section 2.2 at the absorption edges,  $f_1^0$  and  $f_2^0$  undergo sharp variation. Therefore, the optical constants change significantly near the absorption. If there is change in composition of material, density of materials and slight variation in effective electron density, the near edge optical response would vary drastically. The result is analogous to using deuteration as marker in neutron reflectivity, however, without requiring any special sample preparation [74, 75]. Therefore, tuning incident photon energy near absorption edge would make possible the analysis of composition of buried interfaces, formation of native oxide and depth profiling of variation of atomic density in thin film using soft X-ray resonant reflectivity.

Soft X-ray interacts with matter via. elastic scattering, inelastic scattering and photo absorption. Elastic scattering takes place by two different ways: scattering by free electrons (Thomson scattering) and coherent scattering by strongly bound electrons. Inelastic scattering (known as Compton scattering or incoherent scattering) occurs from loosely bound electrons and involves small change in incident photon energy after scattering. Photo absorption occurs when all the energy of incident photon transfers to the inner shell electrons and ionizes the atom. In the soft X-ray region, inelastic scattering is negligible, while the elastic atomic scattering cross section is lower by a factor of  $\sim 10^3$ - $10^4$  than the atomic absorption cross section. Although scattering cross section is much smaller than absorption cross section from a single free atom, if scattered amplitudes by different atoms in an element of matter are added in phase, the total scattered intensity is proportional to the square of the volume of the element, as compared to the total absorbed intensity which is linearly proportional to the volume. As the volume of the element is larger, with increase in volume, the total scattered intensity increases over absorption. For more additional information regarding interaction of soft X-ray with matter, the reader is referred to comprehensive review paper of X-ray microscopy [76, 77].

Figure 2 shows calculated attenuation length (the length at which the intensity reduces to  $1/e$  of original value) of soft X-ray for different materials at normal angle of incidence using Henke et al. database. Again, the atomic-like assumption is clearly a poor approximation in the vicinity of absorption edges (as discussed earlier), Henke et al. data is not sufficient to provide accurate value of attenuation length near the edge, but a rough idea about attenuation length provides information about the thickness of the thin films probed using soft X-ray resonant reflectivity. For Si, the minimum attenuation length near Si L-edge is  $\sim 55$  nm. Similarly for B, the minimum attenuation length near B K-edge is  $\sim 48$  nm. Soft X-ray penetrating power

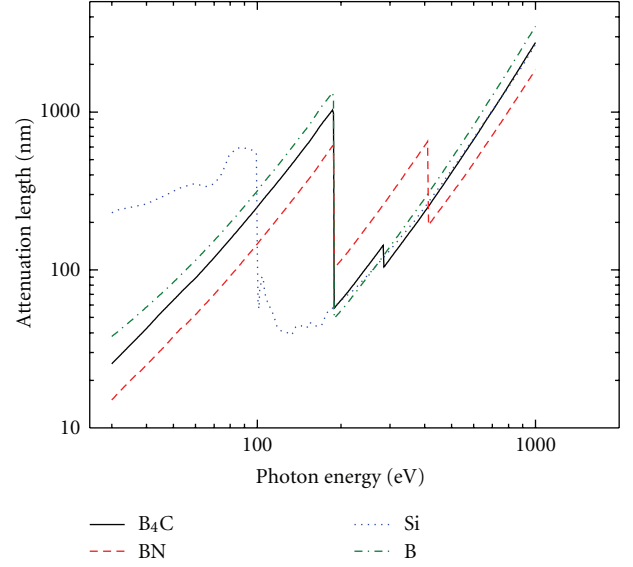


FIGURE 2: Attenuation lengths of soft X-ray under normal angle of incidence in different low-Z elements and their compounds using the Henke et al. database [61].

varies strongly with energy near the absorption edge and with chemical composition. For compounds, the attenuation length is basically higher than the corresponding element due to molecular and condensed matter effect. The limitation of the soft X-ray resonant reflectivity for studying structural parameters of thin films and multilayer structure is that the total film thickness should be less than attenuation length for the corresponding materials near the absorption edge.

**2.4. Scattering/Reflectivity Background.** Let us consider a plane electromagnetic wave with the wave vector  $k_i$  incident from vacuum on a material with a perfectly smooth interface (ideal case) at an angle  $\theta_i$ , as shown in Figure 3. As shown in wave vector scattering diagram, wave vector transfer (also known as momentum transfer vector) is  $q = |\Delta k| = k_r - k_i$ . The Fresnel reflectivity for s-polarized electric field (electric field parallel to plane of incidence) can be written, for incident angle larger than critical angle ( $q_z \gg q_c$ ), as [78]

$$R^s(q_z) = |r^s(q_z)|^2 \approx \frac{|q_c|^4}{16q_z^4}, \quad (5)$$

where  $q_z$  is the z-component of momentum transfer vector from the boundary to the photon  $q_z = 2k_i \sin \theta_i = 4\pi \sin \theta_i / \lambda$  ( $n = 1$  for vacuum) critical values of momentum transfer vector,  $q_c$ , can be written as

$$\begin{aligned} q_c &= \frac{4\pi \sin \theta_c}{\lambda} \approx \frac{4\pi \theta_c}{\lambda} = \frac{4\pi(\sqrt{2\delta})}{\lambda} \\ &= \sqrt{16\pi r_e \rho} = \sqrt{16\pi(\text{SLD})}, \end{aligned} \quad (6)$$

where  $\rho = N_a f_1^0$  is the electron density (number of electrons per unit volume) and  $\text{SLD} = \rho r_e$  is the scattering

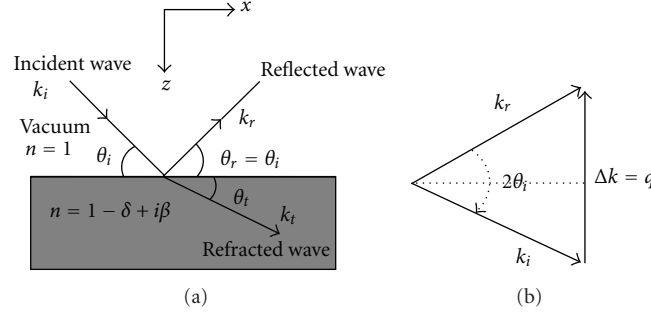


FIGURE 3: (a) Schematic of incident, reflected, and refracted electromagnetic waves at the interface between vacuum and a material with  $n = 1 - \delta + i\beta$ . The plane of incidence contains the incident wave, reflected wave and the normal to the surface. (b) Scattering wave vector diagram.

length density. It is important to mention that (5) is derived assuming the absorption part  $\beta \approx 0$ . However in extreme ultraviolet and soft X-ray region particularly near the absorption edge, this assumption is not valid because of high absorption. Considering absorption and using (6), Fresnel specular reflectivity (5) can be written as

$$R^s \propto \Delta\delta^2 + \Delta\beta^2, \quad (7)$$

where  $\Delta\delta = \delta_1 - \delta_2$  and  $\Delta\beta = \beta_1 - \beta_2$  are the difference in optical constants between two material across interface. The term  $\Delta\delta^2 + \Delta\beta^2$  is the quantitative measure of the optical contrast between two materials. The optical constants of an element near the absorption edge vary rapidly. Again, as the chemical composition of the element changes, the binding energy and the number of effective electron changes significantly, and provides significant differences in optical response compared to pure elemental response near the edge. Both of these features have a significant effect on the optical contrast towards the determination of chemical composition, atomic density profile and low contrast thin film structures such as formation of native oxide. Such an ability of SXRR to recognize layer, chemical and elemental specificities opens the possibility to combine structural with chemical analysis of low  $Z$  thin films and multilayer structures.

In case of multilayer (ML) structure, Fresnel reflection coefficient from a single interface can be extended to ML structure. There are two theories to calculate the reflectivity from such a ML structure, namely the kinematical theory (single scattering approach), also called the first-order Born approximation and dynamical theory. The kinematical theory is valid in the so-called “weak-scattering regime”, that is, when the cross section of scattering is small, and multiple-scattering effects may be neglected [79] (also see ref. [6]). The more exact rigorous theory is the dynamical theory which takes into account multiple scattering. We will proceed with dynamical theory and deduce kinematical theory under appropriate approximations. The dynamical calculation of reflectivity was first formulated by Abeles [80] in 1950 using the matrix method. Equivalent to this formalism is a recursive approach first described by Parratt in 1954 [1] which is the most cited work in the field of

X-ray reflectometry. According to Parratt’s formalism, the recursion relation for the reflected amplitude at the interface between  $j$  and  $(j + 1)$  layer can be written as

$$r_{j,j+1} = \exp(-iq_{j,z}t_j) \frac{f_{j,j+1} + r_{j+1,j+2} \exp(-iq_{j+1,z}t_{j+1,z})}{1 + f_{j,j+1}r_{j+1,j+2} \exp(-iq_{j+1,z}t_{j+1,z})}, \quad (8)$$

where  $f_{j,j+1} = (q_{j,z} - q_{j+1,z})/(q_{j,z} + q_{j+1,z})$  is the Fresnel s-polarised reflection coefficient for the interface between  $j$  and  $j + 1$  layers,  $q_{j,z} = (4\pi/\lambda)(n_j^2 - \cos^2\theta)^{1/2}$  is the normal component of momentum transfer in the  $j$ th layer,  $t_j$  is the thickness of  $j$ th layer and  $n_j$  is the refractive index of the  $j$ th layer. For a multilayer system with  $M$  number of layers on a semiinfinite substrate, the recursion relation starts from the bottom layer with the assumption that  $r_{M,M+1} = 0$ , as the thickness of this medium is assumed to be infinite. One also notes that  $\exp(-iq_{j,z}t_j) = 1$  for  $t = \infty$  and, therefore,  $r_{1,2} = E_1^R/E_1$ . If  $I^R$  and  $I_o$  are respectively the reflected and the incident intensities, then the reflectivity from an ideal ML is  $R = I^R/I_o = |r_{1,2}|^2$ . The structural parameters are obtained by nonlinear least square fitting of measured reflectivity. According to the structure factor of the ML [81], the  $m$ th Bragg peak vanishes if  $m = p/\Gamma$ , where  $\Gamma$  is the ratio of thickness of the high- $Z$  material to the total period thickness and  $p$  is an integer. If ML structure has  $N$  periods, then,  $N - 2$  Kiessig oscillations are observed between two successive Bragg peaks. These Kiessig oscillations arise due to interference of the waves reflected from the vacuum/top layer and bottom layer/substrate interfaces [82].

Although Parratt’s formalism is an exact formula to calculate the reflectivity from thin film ML structure, it is quite cumbersome to use. Furthermore, there is no apparent way to invert this recursive formula to obtain the real structure. However, in practice, Parratt’s formalism is routinely used to model the measured reflectivity data, if it is assumed that the electron density profile is not too complicated and the guessed fitting parameters do not deviate significantly from the actual real structure. The calculated and measured reflectivity profiles are compared with an iterative change in the initial guess. This fitting is not unique if there are large numbers of free parameters. On

the other hand, the kinematical theory of scattering provides an opportunity of inverting the measured reflectivity profile which results in model independent method for obtaining real structure parameters at the cost of several inaccuracies. The kinematical theory of X-ray scattering, is based on the assumption that an incident X-ray photon after being scattered once, is not scattered again. Under this assumption reflectivity is directly related to the Fourier transform of the electron density [83]. The kinematical approach is valid in the so-called “weak-scattering regime” and multiple-scattering effects are neglected [79, 84]. Kinematical theory is not applicable near the critical angle and near Bragg conditions, where multiple scattering cannot be neglected. If the multiple reflection is neglected, the second term in the denominator in (8) is insignificant. The Parratt’s recursion can be rewritten in a slightly different way by replacing  $j + 1$  layer thickness  $t_{j+1}$  by  $\Delta z_{j+1}$ . For convenience, in the integration we write thickness  $t$  in term of  $z$  ( $z$ -component of coordinate system is perpendicular to the sample surface). Then Parratt’s formula (8) can be approximated to

$$r_{j,j+1} \approx f_{j,j+1} + r_{j+1,j+2} \exp(-iq_{j+1,z} \Delta z_{j+1}). \quad (9)$$

By performing recursion in (9), the total reflected amplitude from ML structure can be written as

$$r_{\text{total}} \approx \sum_{j=1}^{M+1} f_{j,j+1} \exp\left(-i \sum_{p=1}^{j-1} q_{p,z} \Delta z_p\right). \quad (10)$$

Total reflected amplitude can be written in terms of electron density by rewriting Fresnel reflection coefficient,  $f_{j,j+1}$ , in terms of electron density using (5) and (6) as

$$r_{\text{total}} \approx 16\pi \sum_{j=1}^{M+1} \frac{\rho_j - \rho_{j+1}}{(q_{j,z} + q_{j+1,z})^2} \exp\left(-i \sum_{p=1}^{j-1} q_{p,z} \Delta z_p\right). \quad (11)$$

Assuming that the momentum transfer vector does not change inside the different layers,  $q_{j,z}(z) = q_{j+1,z}(z)$ , and converting the summation into integration in the continuous limit,  $N \rightarrow \infty$  and  $\Delta z_p \rightarrow 0$ ,  $r_{\text{total}}$  can be written as,

$$r_{\text{total}} \approx 4\pi \int_{-\infty}^{+\infty} \frac{d\rho(z)}{dz} \frac{1}{q_z^2(z)} \exp\left(-i \int_{-\infty}^z q_z(\xi) d\xi\right) dz. \quad (12)$$

If  $q_z \gg q_c$  (far away from critical angle),  $z$ -component of momentum transfer vector inside the layer can be approximated to that of in vacuum, that is,  $q_z(z) \approx q_z$ . So  $1/q_z^2$  can be taken outside of integration. And value of bracketed integration is  $zq_z$ . The Fresnel reflectivity from ML structure in kinematical theory (also known as first-order Born approximation) can be written as

$$R(q_z) = |r_{\text{total}}|^2 = \frac{16\pi^2}{q_z^4} \left| \int_{-\infty}^{+\infty} \frac{d\rho(z)}{dz} \exp(-iq_z z) dz \right|^2. \quad (13)$$

The specular Fresnel reflectivity is related directly to the electron density gradient perpendicular to the sample surface. Thus the Fourier transfer of the specular Fresnel reflectivity data provides information about the corresponding one-dimensional Patterson functions and is used to analyze reflectivity data for structural analysis of low contrast system [10].

So far we considered reflectivity from ideal case. However, in real system, the interfaces are not ideal and have some finite width, caused by imperfections at the interfaces due to roughness, interdiffusion, and chemical reactivity. Contributions from different depths within a boundary will add amplitudes with different phases, resulting in a reduced reflectivity. At the interfaces, the variation of density,  $\rho(z)$ , can be assumed to take the form of an error function. The corresponding gradient of  $\rho(z)$  will be a Gaussian distribution of width  $\sigma$ . Such a Gaussian distribution is obtained when a large number of different periodic amplitudes with random phases are added [63]. The damping of reflectivity due to imperfection at the boundaries is taken into account by multiplying the Fresnel reflectivity by a static Debye-Waller factor [85] considering Nevot and Croce model [86], viz.,  $r_{j,j+1}^{\text{Real}} = r_{j,j+1}^{\text{Ideal}} \exp(-q_{j,z} q_{j+1,z} \sigma_j^2 / 2)$ , where  $\sigma_j$  is the root mean square value of interface roughness between the  $j$ th and the  $(j + 1)$ th layers. An alternative way is that the interface boundaries can be modeled by a series of very thin layer with thickness  $\zeta$  with constant refractive index with sharp interface [87], such that  $\zeta \ll \sigma$ . In addition to this  $\zeta$  must be smaller than  $\pi/q_z^{\text{max}}$ , where  $q_z^{\text{max}}$  is the maximum value of measured  $q_z$ . Then reflectivity can be calculated using Parratt’s formalism with sharp interface. The interface imperfection obtained from specular reflectivity gives information about the surface roughness across the depth of the ML (i.e., not lateral). In the specular case, the scattering wave vector transfer is normal to the sample surface and, hence, only the variation of the electron density along the depth of the ML is obtained, and is laterally averaged over the coherence area of the incident beam. The lateral surface roughness information is obtained from diffuse scattering [88]. In this paper, we have used Parratt’s formalism and interface profile is taken into account using Nevot and Croce model.

### 3. Experimental

B<sub>4</sub>C thin films, Fe/B<sub>4</sub>C bilayers and Mo/Si multilayers (MLs) were deposited using an ultra high vacuum electron beam evaporation system (pressure of  $\sim 2 \times 10^{-9}$  mbar) [89]. A deposition rate of  $\sim 0.6$  nm/min for Mo and Si, and of  $\sim 1$  nm/min for B<sub>4</sub>C and Fe was maintained using a quartz crystal microbalance. The Mo (2.7 nm)/Si (6.3 nm) MLs were fabricated on float glass substrate with 5 layer pairs. B<sub>4</sub>C thin film of 80 nm and B<sub>4</sub>C (60 nm)-on-Fe (18 nm) were deposited on float glass. The surface roughness of float glass used was  $\sim 0.5$  nm. BN thin films are deposited using ion beam sputtering system. Deposition rate was of  $\sim 1.2$  nm/min. The deposition was done at pressure of  $\sim 2 \times 10^{-4}$  mbar. Hard X-ray reflectivity measurements were



carried out using the X-ray reflectometer with a Cu target ( $E = 8047$  eV) [90].

Angle-dependent soft X-ray reflectivity measurements were carried out using vacuum-ultraviolet/soft X-ray reflectometry beamline on Indus-1 synchrotron radiation (SR) source (450 MeV electron storage ring) [91]. The beamline provides a monochromatic photon in the wavelength range of 10–300 eV, using a toroidal grating monochromator (TGM). The resolving power of beamline, that is,  $E/\Delta E$  is in the range of 200–500. The angular resolution of the reflectometer is 0.005 degree. A linear translation stage is used for mounting the sample holder that in turn is mounted on the sample rotation axis. This feature enables the measurement of direct beam intensity as sample can be retracted from the beam path. Detector arm of 200 mm length is used where a silicon photodiode detector is mounted. The base pressure inside the chamber is limited in the range of  $5 \times 10^{-7}$  mbar due to presence of goniometer, stepping motors, electrical wire, and so forth. To withstand the vacuum requirement of beamline, that is,  $1 \times 10^{-9}$  mbar, a differential pumping system is installed. In present configuration, the dynamic range of five orders is obtained. The present measurements were performed in the s-polarized geometry.

The XPS study was carried out using photoelectron spectroscopy workstation coupled to a photo electron spectroscopy beamline on Indus-I SR source. This workstation is equipped with an OMICRON 180° hemispherical analyzer (model EA 125) along with twin anodes X-ray (Al  $K_\alpha$  & Mg  $K_\alpha$ ) radiation sources. The concentric hemispherical analyzer with pass energy 50 eV, the overall resolution, including the analyzer, was estimated to be 0.8 eV. The measurements were carried out in a base pressure of better than  $5 \times 10^{-10}$  mbar. The energy scale was calibrated using Fermi level and peak position from the system database. Au  $4f_{7/2}$  at  $84.0 \pm 0.1$  eV served as an external reference. Since the glass substrate is nonconducting, charging effect was observed. To correct the shifts in binding energy of core levels due to charging effect, graphitic C 1s at 284.7 eV was used as an internal reference. Core level spectra were curve fitted after background subtraction. For the depth profiling of the MLs, argon ions of energy of 2.5 KV at 45° angles to sample surface were used. The approximate sputtering rate 2 Å/min for Si and 1.5 Å/min for Mo was determined from an experiment carried out on the known thickness of Mo and Si thin film.

## 4. Results and Discussions

**4.1. Near Edge Optical Response of Low-Z Materials.** At first we discuss the optical response of low-Z materials and their compounds especially near the absorption edge in extreme ultra violet/soft X-ray region. The idea of optical response near the edge provides information about possibility of exploring soft X-ray resonant reflectivity. Also the reliable determination of optical constant near the absorption edge provides a right way for modeling of X-ray multilayer optics for optimum performance [92–97]. Figure 4 shows optical constant ( $\delta$  and  $\beta$ ) in the energy range from 165 to 205 eV for boron (B), boron carbide ( $B_4C$ ) and boron nitride

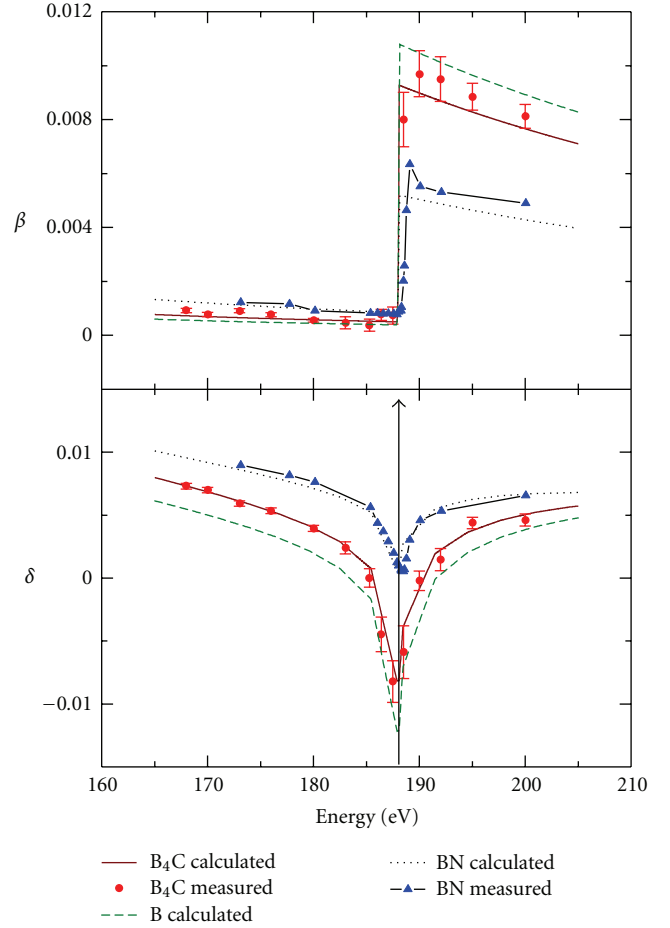


FIGURE 4: The energy dependent optical constants for  $B_4C$ , B, and BN as function of photon energies near the boron K-absorption edge.

(BN) calculated using Henke et al. [61] atomic scattering database and measured values are obtained from best fit from angle dependent soft X-ray reflectivity measurements. The advantage of angle dependent X-ray reflectivity to determine optical constant is that both  $\delta$  and  $\beta$  are obtained simultaneously and independently [98] (also see ref. [66]).

Figure 5 shows soft X-ray reflectivity profile (both measured and fitted) of  $B_4C$  thin film at selected photon energies near B K-edge. From these measurements, optical constant are determined. For the soft X-ray fitting, the structural parameters (such as thickness  $\sim 80.5$  nm, density  $\sim 96\%$  of bulk value and roughness  $\sim 1.2$  nm), obtained from hard XRR, were used and the optical constant ( $\delta$  and  $\beta$ ) are taken from the calculated values given in Figure 4 as the starting guess. Final values of optical constants are obtained from the best fit of the measured reflectivity profile and are given in Figure 4. In Figure 5, the amplitude of the intensity modulation is clearly visible for entire  $q_z$  values at 180 eV due to the interference of reflected beam from vacuum/ $B_4C$  and  $B_4C$ /substrate interfaces. At 185.3 eV, there is no observable amplitude of the intensity modulation. At this energy,  $\delta \approx 0$  and  $\beta \approx 0$  for  $B_4C$  (Figure 4), which is close to the refractive

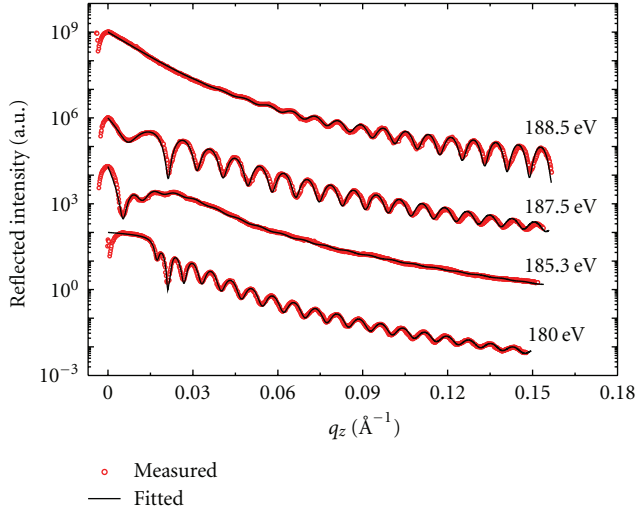


FIGURE 5: Soft X-ray reflectivity spectra of  $B_4C$  80.5 nm thin film for different photon energies at boron K-absorption edge. The optical constants are derived from the best fit.

index for vacuum ( $\delta = 0$  and  $\beta = 0$ ). At this energy  $B_4C$  becomes almost invisible and reflection takes place only from the substrate. At 187.5 eV, the amplitude of intensity modulation reappears due to reflection from vacuum/ $B_4C$  and  $B_4C$ /substrate interfaces. At this energy, the amplitude of the intensity modulation is large due to good optical contrast between the interfaces. As the energy increases further, the absorption in the layer increases significantly (for 188.5 eV) and amplitude of intensity modulation are observed at higher  $q_z$  values. The steep fall of reflected intensity at the critical angle is clearly observed for 180 eV due to total external reflection phenomena and low absorption in the layer at this energy. In the anomalous range where real part of refractive index ( $1 - \delta$ ) is positive (for 187.5 eV and 188.5 eV), total external reflection does not occur at any angle, and hence no critical angle is observed.

In the vicinity of boron K-absorption edge ( $E = 187.7$  eV), the optical constant of B,  $B_4C$  and BN change rapidly as a function of photon energy. There is a sharp jump in  $\beta$  for all three materials while the dispersion term of optical constant ( $\delta$ ) dips to a negative value near the K-edge for B and  $B_4C$ . This is due to sign reversal of real part of forward atomic scattering factor  $f_1^0$ . For BN,  $f_1^0$  does not exhibit sign reversal effects. Far away from boron absorption edge, measured optical constants (for  $B_4C$  and BN) agree with Henke et al. within an error of  $\sim 7\%$ . At the absorption edge, the optical constants of  $B_4C$  deviate by  $\sim 38\%$  from the tabulated values of Henke et al. Similarly for BN, at the absorption edge, the optical constants deviate by  $\sim 82\%$  from the tabulated values of Henke et al. Significant variations of measured optical constants near the edge from Henke tabulated values cannot be accounted by the finite resolution of the spectrometer. This was checked by simulating the reflectivity profile with the tabulated values taking finite energy resolution of the spectrometer. However, better energy resolution of the spectrometer, will

further improve the measured values. At the absorption edge, due to the missing oscillator strength the tabulated optical constants may be inaccurate [66]. The atomic-like assumption is a poor approximation in the vicinity of the absorption edges due to chemical environment. Thus the Henke et al. formalism is not sufficient to establish the details of the dispersion at the edges where the tabulated data are extrapolated near the edge and do not account for molecular and condensed matter effects. In the Henke et al. data, there is no relative shift of absorption edge in the tabulated optical constants of compound  $B_4C$  and BN with respect to B (see Figure 4) which is expected due to change in chemical environment around B in case of compounds. We observed the shift in absorption edge in the measured optical constants of compounds (see Figure 4). The measured shift in absorption edge for  $B_4C$  and BN are  $\sim 0.5$  eV and  $\sim 0.8$  eV, respectively with respect to pure B. Assuming stoichiometric  $B_4C$  and BN, this shift in absorption edge with respect to pure B may be associated with the electronic transition from a B 1s state into unoccupied B 2p states. This transition energy can also vary slightly from nonstoichiometric  $B_4C$  and BN or for boron oxide [99]. In both the compounds, due to the higher electronegativity of bonding partner, the electronic charge density near boron atom is reduced. Therefore, in comparison to elementary boron, the B 1s peak is shifted to higher energies with carbon and nitrogen as its neighbor. The higher shift of absorption edge in case of BN may be due to stronger covalent bond in BN due to more electronegativity of nitrogen than carbon. Further this may be one of reason that BN does not exhibit sign reversal of  $f_1^0$  whereas  $B_4C$  does. Ksenzov et al. [99] have measured optical constants of  $B_4C$  near B K-edge using refraction correction method of Bragg diffraction from sputtered deposited Ru/ $B_4C$  multilayer. They have also observed similar significant variation in optical constants near the boron edge with respect to Henke's tabulated value, sign reversal of  $f_1^0$  as well as shift of absorption edge towards higher energy side. Soufli et al. [98] report measured optical constants in soft X-ray region for sputter deposited  $B_4C$  thin film and the values near the boron K-edge deviate significantly from the tabulated values by Henke et al. Furthermore, they also report sign reversal for  $\delta$  around the boron edge as well as shift in absorption edge towards higher energy side. The sign reversal effect of  $f_1^0$  near B K-edge is also observed experimentally in case of boron [100]. For BN, to the best of our knowledge, we present here for the first time the measured optical constants near the boron K-edge. Earlier, Hoffman et al. [101] studied optical properties of pyrolytic BN in the energy range 0.05–10 eV. Similarly, Miyata et al. [102] measured optical constants of cubic BN in the vacuum ultraviolet region ( $\sim 2$ –20 eV). Infrared optical constants of polycrystalline BN is studied by Khelkhal and Herlemont [103]. Similarly Yixi et al. [104] measured vacuum ultraviolet reflectance spectra and determined optical constants in the energy range 5–12 eV of wurtzite BN by applying the Kramers-Kronig relation.

Figure 6 shows the optical constants calculated in the wavelength range 95 to 105 eV for Mo, Si and different silicide compositions, using the Henke et al. atomic

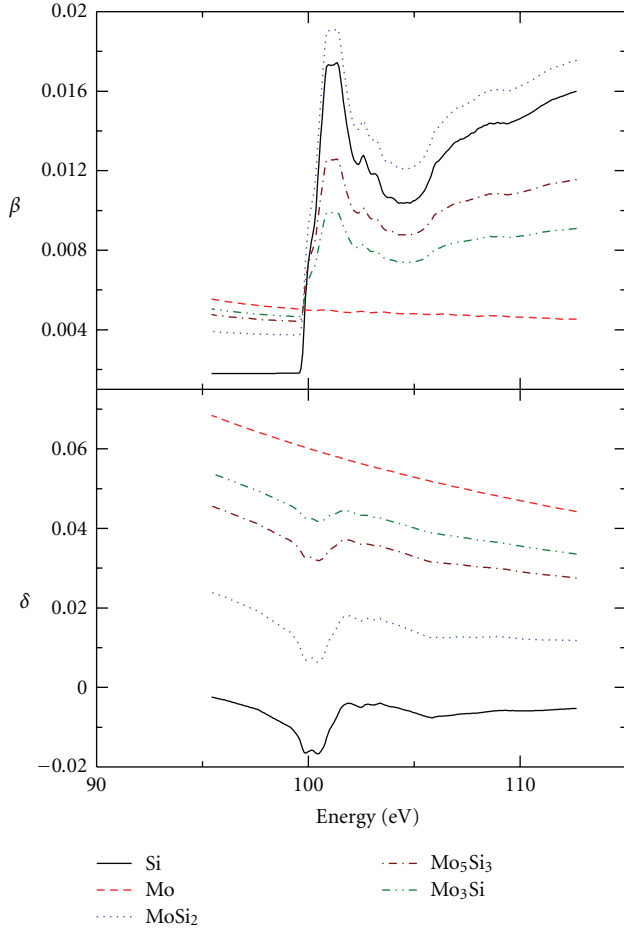


FIGURE 6: Calculated optical constants for Mo, Si, MoSi<sub>2</sub>, Mo<sub>5</sub>Si<sub>3</sub>, and Mo<sub>3</sub>Si as function of photon energy near the Si L-absorption edge.

scattering database. Optical constants of silicides are calculated using densities of MoSi<sub>2</sub>, Mo<sub>5</sub>Si<sub>3</sub>, and Mo<sub>3</sub>Si as 6.24, 8.24 and 8.968 gm/cm<sup>3</sup>, respectively [105], and weighted averages of atomic scattering factors. In the vicinity of Si L-edges ( $L_{II} \approx 100.4$  and  $L_{III} \approx 99.83$  eV) (regions of anomalous dispersion), the optical constants ( $\delta$  and  $\beta$ ) of Si and its different silicide compositions change rapidly as a function of photon wavelength. In general, the fine structures of the optical constants near absorption edges depend on the composition of the phases. It is also clear from Figure 6 that the three silicide phases (MoSi<sub>2</sub>, Mo<sub>5</sub>Si<sub>3</sub>, and Mo<sub>3</sub>Si) of varying Si content display markedly different optical constants at the edge and that the optical contrast is sufficiently large. This enables the observation of changes in reflectivity patterns from buried interfaces.

Since the reflected intensity as a function of scattering vector ( $q_z$ ) of a real structure and the extent of the interference oscillations depends on the relative Fresnel reflection coefficient at each interface between two materials ( $\propto \Delta\delta^2 + \Delta\beta^2$ , scattering strength) the reflectivity from a particular interface can be selectively tuned using the fine structure features of energy dependent optical constants.

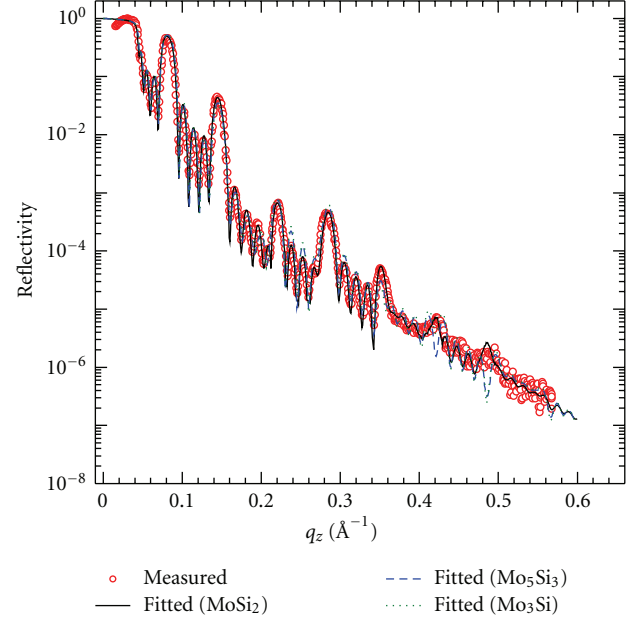


FIGURE 7: Measured X-ray reflectivity profile (at  $E = 8047$  eV) along with simulated profile of [Mo (2.7 nm)/Si (6.3 nm)]<sub>5</sub> ML.

Through the use of the specific energies, that provides the maximum optical contrast, the sensitivity of a particular interface can be selectively enhanced. In the subsequent subsections, we discuss the possibility of exploring soft X-ray resonant reflectivity for the analysis of different structural parameters of thin films and multilayer structures of low- $Z$  materials with enhanced sensitivity.

**4.2. Determination of Interlayer Composition.** In this subsection, we explore soft X-ray resonant reflectivity (SXRR) to analyze interlayer composition at buried interfaces with subnanometer sensitivity. Although the principle is applicable in general to any multilayer system near the resonant absorption edges, here we demonstrate the technique through characterization of Mo/Si multilayer (ML) system [106, 107] using simulation and experiment. Before moving to SXRR, we show the difficulty in probing such low contrast interlayer composition using conventional hard XRR method. Figure 7 shows the hard XRR of Mo/Si ML used in the present study with periodicity  $d = 9$  nm and number of layer pairs,  $N = 5$ . The successive higher order Bragg peaks (upto 7th order) and distinct  $N - 2$  number of Kiessig oscillations between peaks in the measured data reveal the good quality of the ML structure. The observed regular Kiessig oscillations between successive Bragg peaks in the data indicate that the statistical thickness errors of the layers are small. The  $R(q_z)$  calculated taking statistical fluctuations of the layer thickness show that the mean thickness error is below one percent of the periodicity.  $\Gamma$  (ratio of Mo thickness to the period thickness) was intentionally kept at 0.3 to verify absence of peaks of the 3rd order and its multiples. The presence of these peaks in the data indicates that the effective  $\Gamma$  value changes due to the formation of an interlayer compound. The interlayer is due

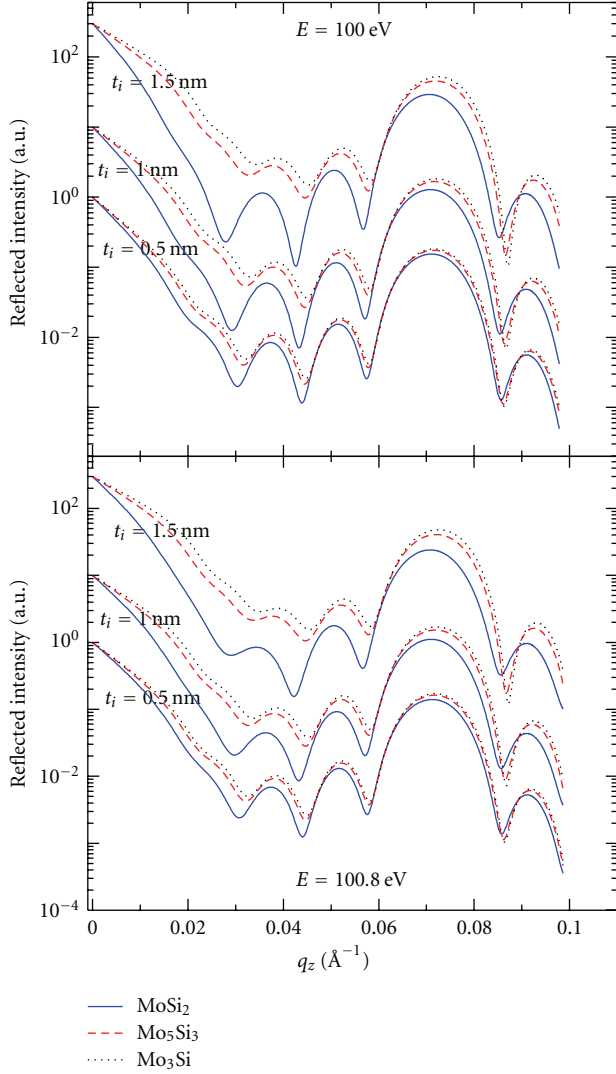


FIGURE 8: Simulated soft X-ray reflectivity profile of  $[\text{Mo (2.7 nm)/Si (6.3 nm)}]_5$  ML structure at selected photon energies at Si L-edge.

to mixing between Mo and Si. Experimental data are fitted using Parratt's formalism based on a nonlinear least squares-fitting algorithm. The structural parameters (thickness  $t$  and roughness  $\sigma$ ) obtained from best fit results are  $t_{\text{Si}} = 4.7 \pm 0.1$  nm with  $\sigma = 0.5$  nm; Si-on-Mo interlayer,  $t_{\text{Si-on-Mo}} = 0.8 \pm 0.1$  with  $\sigma = 0.5$  nm;  $t_{\text{Mo}} = 2.4 \pm 0.1$  with  $\sigma = 0.6$  nm; Mo-on-Si interlayer,  $t_{\text{Mo-on-Si}} = 1.0 \pm 0.1$  with  $\sigma = 0.45$  nm. The interlayer optical constants are  $\delta = 19.1 \times 10^{-6}$  and  $\beta = 11.6 \times 10^{-7}$ . The best fit result also suggest the formation of a native oxide of 1.2 nm thickness with roughness 0.5 nm on the top Si layer of the ML structure. The model fitted data for three possible (different) interlayer phase compositions [108] show that conventional XRR is not sensitive to the interlayer composition formed at buried interface. This is due to the small difference in optical constants among these compositions.

The effect of energy-dependent optical constants on reflectivity profile near the Si L-edge is illustrated in Figure 8

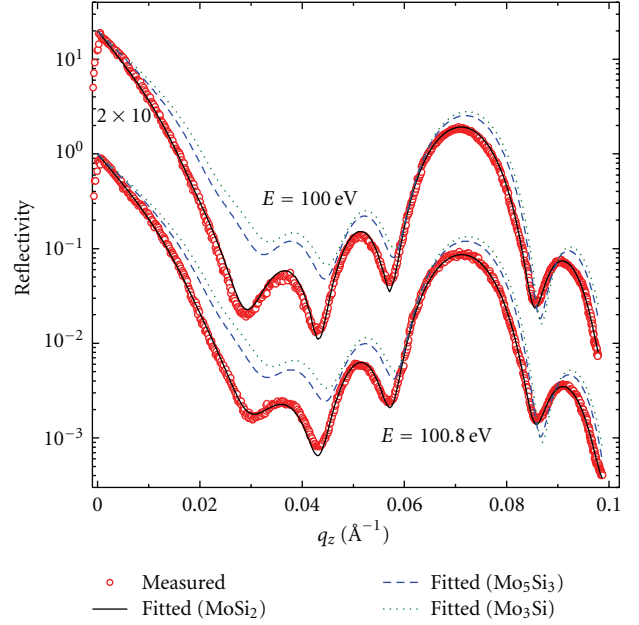


FIGURE 9: Measured soft X-ray reflectivity of  $[\text{Mo (2.7 nm)/Si (6.3 nm)}]_5$  ML at the same photon energies as simulated in Figure 8. The best fit is obtained for  $\text{MoSi}_2$  composition.

for an ideal (without roughness) Mo/Si ML structure at selected energies. The simulations are performed with changing interlayer compositions ( $\text{MoSi}_2$ ,  $\text{Mo}_5\text{Si}_3$ , and  $\text{Mo}_3\text{Si}$ ) as well as interlayer thickness ( $t_i$ ) from 0.5 to 1.5 nm. For the simulation we have used, Mo/Si ML period  $d = 9$  nm, the number of layer pairs  $N = 5$  and the  $\Gamma = 0.3$ . The reflectivity profile can clearly distinguish three different compositions and interlayer thickness even on a subnanometer scale. The refraction changes the angle of propagation of the radiation entering the ML and therefore changes the angular position of Bragg peak for different compositions.

Figure 9 shows the soft X-ray resonant reflectivity measured near the Si L-edge energy. The experimental data are fitted for three different compositions, that is,  $\text{MoSi}_2$ ,  $\text{Mo}_5\text{Si}_3$  and  $\text{Mo}_3\text{Si}$ . For the fitting, the structural parameters obtained from XRR (given above) are used, and the optical constants ( $\delta$  and  $\beta$ ) taken from Figure 6 as the starting guess for simulation. The measured reflectivity profile shows an overall trend similar to that in the simulations. For two different photon energies, good agreement between measured and best fit curve is obtained for the  $\text{MoSi}_2$  composition, not only near the Bragg peak but also in the Kiessig oscillation regions and at grazing angles of incidence around the critical angle. The amplitude of the intensity modulation is smaller at  $E = 100.8$  eV than at  $E = 100$  eV, which is due to increase in the effective electron density, which in turn depends on the real part of the atomic scattering factor  $f_1^0$ . The best fit results are tabulated in Table 1. At  $E = 100$  eV and 100.8 eV, the optical constants  $\delta$  and  $\beta$  value for Si and  $\text{MoSi}_2$  differ significantly from those calculated from Henke et al. database [61], given in Figure 6. For Mo, both  $\delta$  and  $\beta$  values agree well with Henke's values



TABLE 1: The best fit results of soft X-ray resonant reflectivity measurements on Mo/Si ML with MoSi<sub>2</sub> composition at interfaces obtained tuning photon energy at Si L-edge. In square bracket the tabulated values of  $\delta$  and  $\beta$  from Henke et al. [61].

Energy (eV)	$\delta_{\text{Si}}$	$\beta_{\text{Si}}$	$\delta_{\text{Mo}}$	$\beta_{\text{Mo}}$	$\delta_{\text{MoSi}_2}$	$\beta_{\text{MoSi}_2}$	R (%)
100.8	-0.012 [-0.014]	0.015 [0.0167]	0.058 [0.0589]	0.004 [0.005]	0.007 [0.0089]	0.017 [0.0184]	8.6
100	-0.015 [-0.0163]	0.007 [0.0066]	0.060 [0.0603]	0.005 [0.005]	0.008 [0.0071]	0.0092 [0.0085]	9.3

(within experimental error) for the two different energies. The fitted curves for Mo<sub>5</sub>Si<sub>3</sub> and Mo<sub>3</sub>Si deviate significantly from the measured data.

The observed results obtained from soft X-ray resonant reflectivity are correlated with depth profile XPS measurements performed using an Al K $\alpha$  source. The survey scans of the Mo/Si ML sample without sputtering indicates the presence of adsorbed oxygen and carbon on the top surface. The survey scans corresponding to sample sputtered for 15 minutes showed reduction of O 1s and C 1s peaks below the detection limits (a few atomic percentages). These results indicate that the interfaces are not contaminated. The narrow scans of Mo 3d spectrum for different sputtering times are shown in Figure 10 along with the simulated profiles. To calibrate the chemical shift at the interface, XPS spectra of Mo thin films are shown at top of Figure 10. The fitted Mo 3d spectrum corresponding to virgin sample shows no signal from Mo, since Si is the top surface. After 15 minutes sputtering, peaks at binding energy 227.5 eV and 230.7 eV are observed. These peaks can be assigned to Mo 3d<sub>5/2</sub> and Mo 3d<sub>3/2</sub> of MoSi<sub>2</sub>, respectively. During fitting all possible Mo-Si compounds are taken into account. Thus, it can be seen from the analysis of Figure 10 that MoSi<sub>2</sub> is the majority compound at the Mo/Si interfaces. With increase in sputtering time, there is a increase in Mo contribution from pure Mo (B.E. 227.9 eV and 231.02 eV for Mo 3d<sub>5/2</sub> and Mo 3d<sub>3/2</sub>, resp., given at top of Figure 10) and MoSi<sub>2</sub>. At the first interface (Si-on-Mo), the maximum contribution of Mo is from MoSi<sub>2</sub>. The shift in the Mo 3d<sub>5/2</sub> and Mo 3d<sub>3/2</sub> peaks are  $\sim 0.4 \pm 0.04$  eV, with respect to pure Mo, towards lower binding energy. As the sputtering time increases (35 minutes), the Mo contribution from pure Mo increases and of MoSi<sub>2</sub> decreases. Similarly, we have seen, at the second interface (Mo-on-Si), shift in the Mo 3d<sub>5/2</sub> and Mo 3d<sub>3/2</sub> peaks are  $\sim 0.4 \pm 0.04$  eV, with respect to pure Mo, towards lower binding energy [109]. The Mo 3d peaks shift by  $\sim 0.4 \pm 0.04$  eV towards lower binding energy with respect to pure Mo, suggest the formation of the MoSi<sub>2</sub> phase [106] at both the interfaces. This result agrees well with the composition obtained using nondestructive soft X-ray resonant reflectivity. Our results of MoSi<sub>2</sub> composition at interfaces of Mo/Si ML system agrees well with previously reported results using transmission electron microscopy [107].

**4.3. Depth Profiling of Atomic Density.** As we discussed earlier the atomic scattering factors undergoes strong variation near the absorption edge of an element. This provides the high and tunable scattering strength,  $\Delta\delta^2 + \Delta\beta^2$ , at the interface. If the atomic density (porosity) of a material changes, it effects electron density in the material. This should

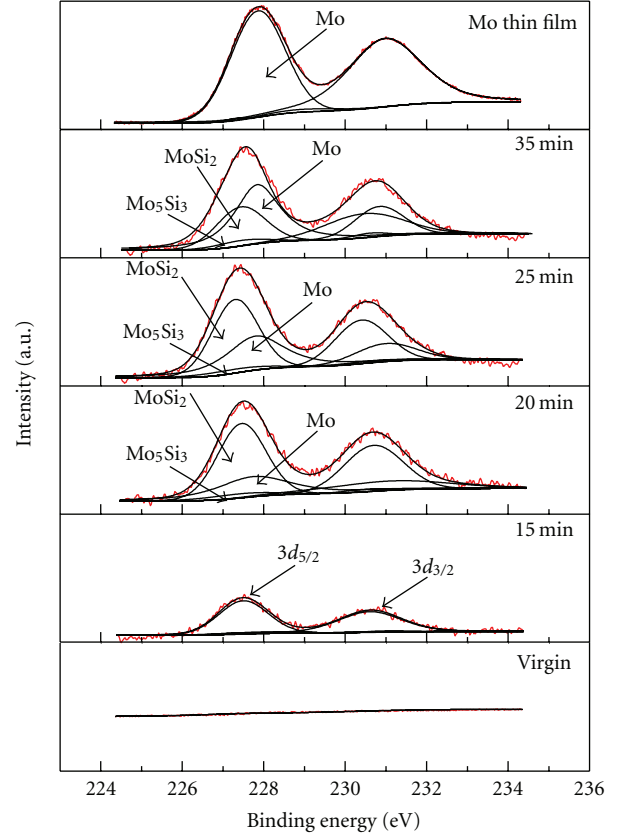


FIGURE 10: XPS narrow scans for Mo 3d peak using Al K $\alpha$  energy of Mo/Si ML for different sputtering time.

generate variation in scattering strength. If the percentage change in atomic density is small, it is difficult to study porosity using XRR due to low optical contrast. However, this problem is overcome by exploiting resonant reflectivity due to resonance enhancement of optical contrast. In this subsection, we demonstrate the sensitivity of SXRR to in-depth variation of porosity (both depth profiling as well as percentage of porosity) in thin layer of resonating material. We demonstrate the idea through characterization of B<sub>4</sub>C-on-Fe bilayer near B K-edge using both simulation and measurements. Before SXRR study, the B<sub>4</sub>C-on-Fe bilayer is characterized using XRR.

The measured XRR profile of B<sub>4</sub>C-on-Fe bilayer at 8047 eV along with the simulated profile is shown in Figure 11. The inset shows electron density profile (EDP) of the film (continuous line), obtained from the best fit XRR profile. The dotted line represents bulk electron density for Fe and B<sub>4</sub>C. The best fit XRR results reveal, 17.2 nm Fe layer with root mean square (rms) roughness  $\sim 0.6$  nm. The

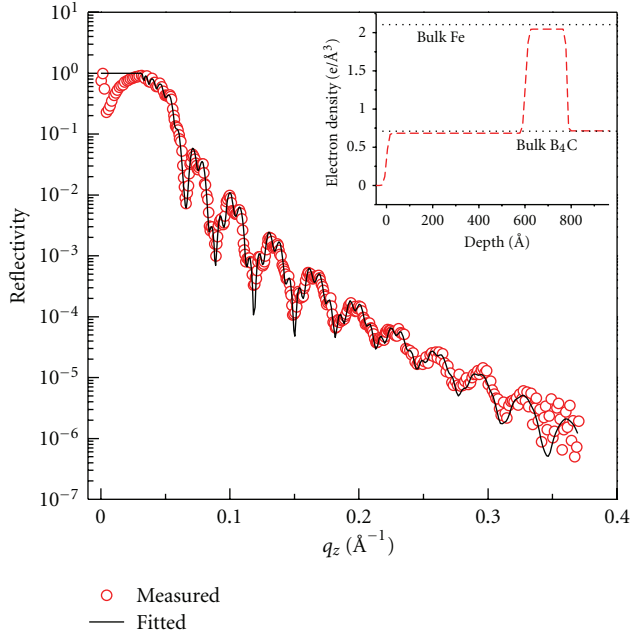


FIGURE 11: XRR spectrum of  $B_4C$  (60 nm) on Fe (18 nm) bilayer film at 8047 eV. In the inset, the continuous line shows EDP profile of the bilayer and the dotted line shows bulk values.

$B_4C$  layer thickness is 59.6 nm with rms roughness  $\sim 0.8$  nm. The average electron density of pure Fe layer is  $2.05 \text{ e}/\text{\AA}^3$ , which is  $\sim 97\%$  of the bulk value ( $2.109 \text{ e}/\text{\AA}^3$ ). Similarly, the average electron density of pure  $B_4C$  layer is  $0.67 \text{ e}/\text{\AA}^3$ , which is  $\sim 95\%$  of the real bulk value ( $0.713 \text{ e}/\text{\AA}^3$ ). The best fit results give qualitative indication of the presence of  $\sim 1.3$  nm porous  $B_4C$  layer in pure  $B_4C$  layer. However, there is significant uncertainty in the percentage of porosity and position of the porous layer. XRR simulated profiles are almost identical with change in porosity upto  $\sim 35\%$  and position of the porous layer at different position in pure  $B_4C$  layer. Simulated reflectivity profile is almost identical to the one due to change in roughness (Figure 12). The difficulty towards obtaining quantitative information of this porous layer using conventional XRR is due to weak scattering contrast between pure  $B_4C$  and porous  $B_4C$  layer. To overcome this difficulty, we propose the possible use of SXRR, which allows sufficient scattering contrast by tuning incident photon energy.

Figure 13 shows a comparison of the scattering strength,  $\Delta\delta^2 + \Delta\beta^2$ , at different interfaces near B K-edge. In Figure 13(a), we show scattering strength at the interface between Fe with  $B_4C$  considering different mass densities. Just near the edge, as the density of  $B_4C$  changes the scattering strength changes significantly. Thus, if there is presence of  $B_4C$  layer with different density at the interface between Fe and  $B_4C$ , the scattering contrast undergoes significant changes which will be reflected through reflected profile. Figure 13(b) shows scattering strength at interface between  $B_4C/B_4C$  with different densities and vacuum/ $B_4C$  with different densities. Just near the edge, the scattering strength changes significantly at the interfaces of  $B_4C$  with different

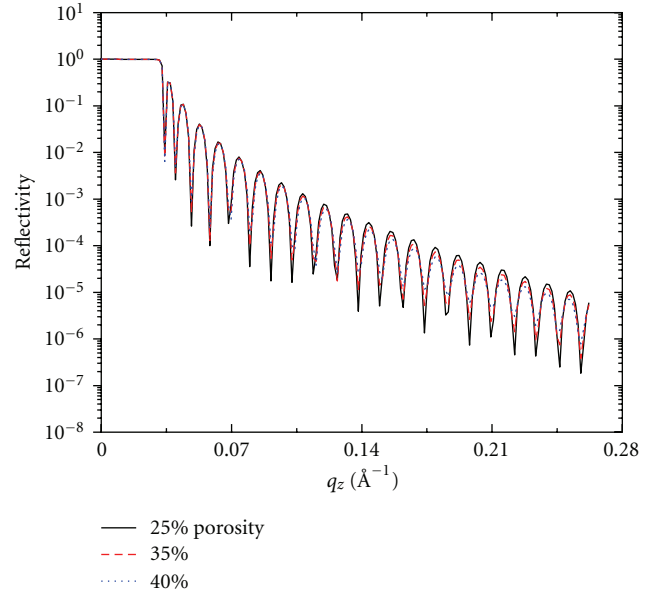
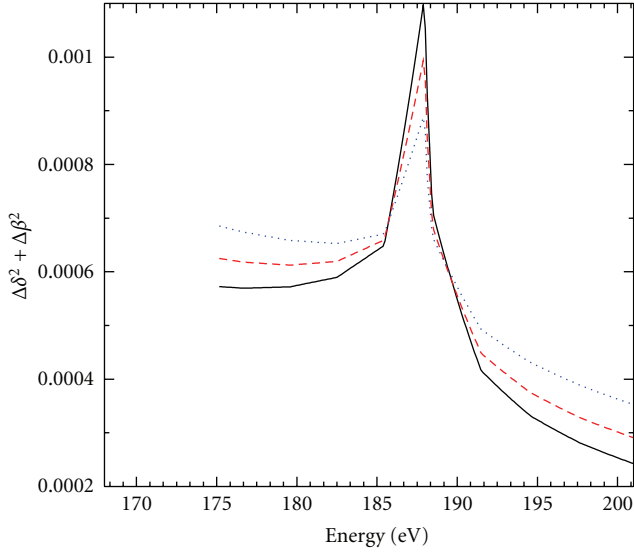


FIGURE 12: Simulated XRR profile (at 8047 eV) of  $B_4C$  (60 nm) thin film with a 1.3 nm porous  $B_4C$  layer with different porosity at the bottom of the film.

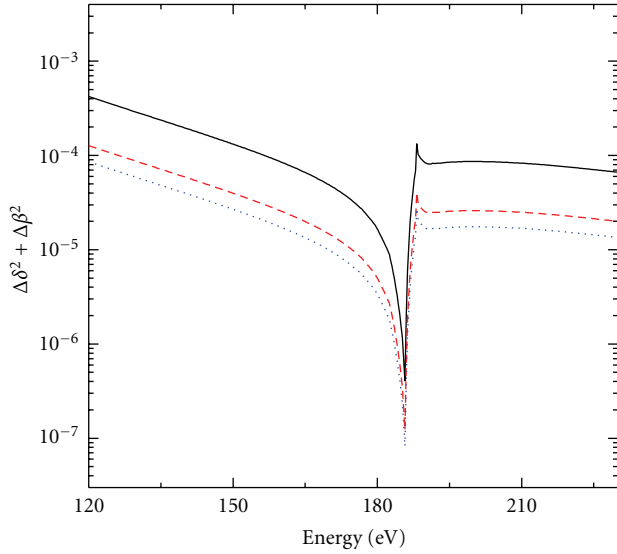
atomic density as well as at interface between vacuum and  $B_4C$  with different densities. Thus if top  $B_4C$  layer is of different density, it gives change in scattering contrast with respect to vacuum. Similarly it also gives change in scattering contrast at the interfaces of same materials with different densities. The scattering strength is sufficient to observe the effect in reflected profile if the density of the material changes at the top of the film, inside the material or at the interface with other materials. Hence, the calculated scattering strength at the interfaces of materials with different density provides an idea of possibility of probing porosity in thin films through resonant reflectivity profile which has been demonstrated at below using both simulations and experiments.

For probing selected interface containing resonating atom with varying density, simulations are performed at the selected photon energy near the boron K-absorption edge. The effect of change in porosity of boron carbide thin layer and the position of the layer are simulated. The effect on the reflectivity profile due to the presence of 1.3 nm boron carbide porous layer in 60 nm boron carbide thin films is shown in Figure 14. Figure 14(a) shows the depth sensitivity of porous layer with 35% of porosity. The reflectivity profile gets redistributed with change in position of the porous layer. With change in position of the porous layer there is a significant difference in reflected profile even near the critical angle (the inset to Figure 14(a)). Figure 14(b) shows the effect of porosity variation, keeping the porous layer thickness constant. As the porosity increases, the oscillations in reflectivity profile decreases. Furthermore, as the atomic density of resonating boron atom decreases, the maxima of the oscillation get shifted to the higher angle. Similar effect of



— Fe/B<sub>4</sub>C (2.52 gm/cm<sup>3</sup>)  
 - - Fe/B<sub>4</sub>C (2 gm/cm<sup>3</sup>)  
 ..... Fe/B<sub>4</sub>C (density 1.5 gm/cm<sup>3</sup>)

(a)

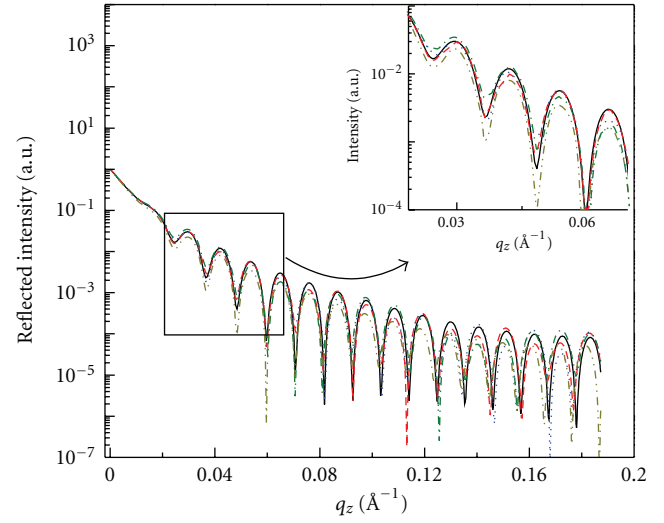


— Vacuum/B<sub>4</sub>C (2.52 gm/cm<sup>3</sup>)  
 - - Vacuum/B<sub>4</sub>C (1.5 gm/cm<sup>3</sup>)  
 ..... B<sub>4</sub>C (2.52 gm/cm<sup>3</sup>)/B<sub>4</sub>C (1.5 gm/cm<sup>3</sup>)  
 - · - · B<sub>4</sub>C (2.52 gm/cm<sup>3</sup>)/B<sub>4</sub>C (1.5 gm/cm<sup>3</sup>)

(b)

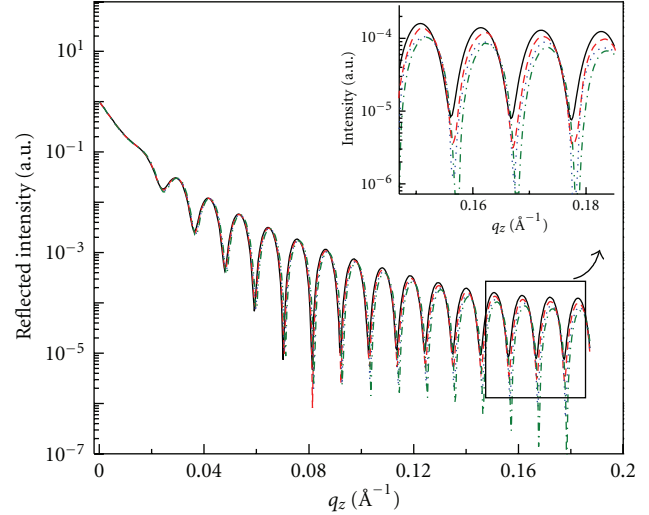
FIGURE 13: Comparison of the scattering strength,  $\Delta\delta^2 + \Delta\beta^2$ , at different interfaces near B K-edge. (a) Fe with B<sub>4</sub>C with different mass densities. (b) B<sub>4</sub>C/B<sub>4</sub>C with different densities and vacuum/B<sub>4</sub>C/with different densities.

reflected profile has been observed in case of simulation on B<sub>4</sub>C (60 nm)-on-Fe (18 nm) bilayer with different position of 1.3 nm porous layer (1.3 nm) with porosity 35% as shown in Figure 15. The significant variations in simulated resonant reflectivity profile with change in the porous layer parameters clearly demonstrate the utility of resonant scattering



— At bottom  
 - - At 20 nm  
 ..... At 30 nm

(a)



— 0% porosity  
 - - 20%  
 ..... 40%  
 - · - · 60%

(b)

FIGURE 14: Simulated reflectivity profile at 187.5 eV for 60 nm B<sub>4</sub>C thin film with a low density B<sub>4</sub>C layer of 1.3 nm (a) depth sensitivity with porosity 35%. (b) Sensitivity to porosity.

measurements towards probing variation of resonating atomic density in buried interfaces.

SXRR measurements of B<sub>4</sub>C-on-Fe bilayer at selected photon energies are shown in Figure 16 along with the fitted profiles. The values of roughness, thickness and density of the films obtained from XRR are used in the soft X-ray model fitting. For soft X-ray data fitting, the optical constants for B<sub>4</sub>C are taken from measured values (Figure 4). The optical constants ( $\delta$  and  $\beta$ ) for the substrate and

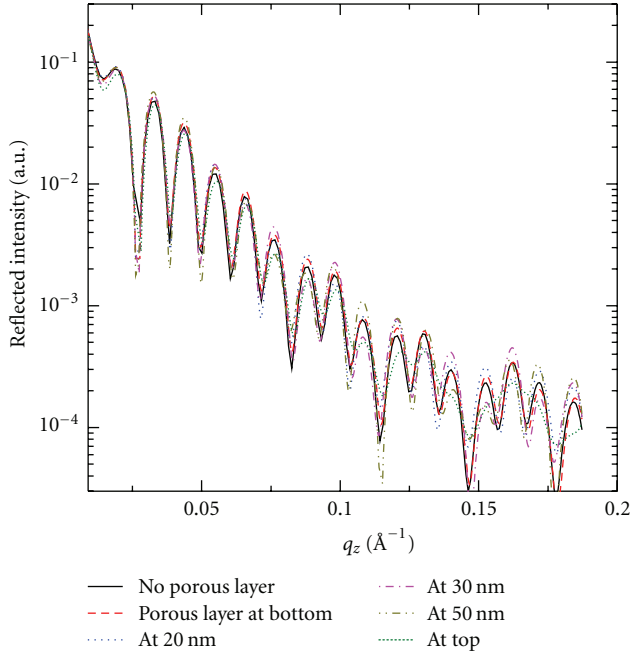


FIGURE 15: Simulated reflectivity profile at 187.5 eV for  $B_4C$  (60 nm)-on-Fe (18 nm) bilayer, with porous  $B_4C$  layer. The thickness of porous layer is 1.3 nm with porosity 35%.

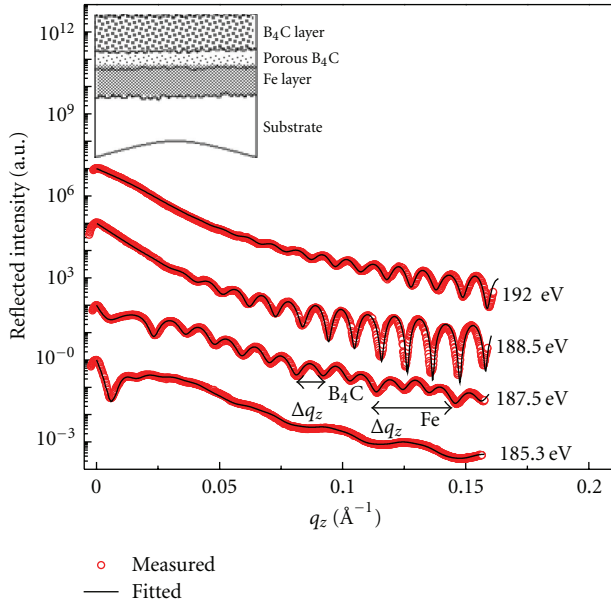


FIGURE 16: SXRR profiles of  $B_4C$  on Fe bi-layer film near boron K-absorption edge. Solid circles represents experimental data continuous line represents the fitted value. The inset shows the model.

Fe are the Henke tabulated values, and have not been varied during the fitting of reflectivity profiles in soft X-ray region. Here we have assumed that significantly away from the absorption edge of the constituent elements, the Henke's tabulated values are reasonably reliable. The best fit results are tabulated in Table 2. At 185.3 eV, optical

constants  $\delta \cong 0$  and  $\beta \approx 0$  for  $B_4C$  (Table 2). This corresponds to optical constants for vacuum ( $\delta = 0$  and  $\beta = 0$ ). As a consequence,  $B_4C$  layer is virtually invisible. The single film oscillation pattern is due to interference of reflected beam from substrate/Fe and Fe/virtually invisible  $B_4C$  interfaces. There is insignificant reflected intensity at Fe/ $B_4C$  interface, showing poor sensitivity towards Fe/ $B_4C$  interface. At 187.5 eV, high sensitive to Fe/ $B_4C$  interface is evident through strong modulations in the reflectivity profile (Figure 16). At this energy, modulations in the reflectivity profile arise from substrate/Fe, Fe/ $B_4C$  and  $B_4C$ /vacuum interfaces. The high frequency oscillations with  $\Delta q_z^{B_4C} = 0.011 \text{ \AA}^{-1}$  corresponding to  $B_4C$  layer which gets modulated over low frequency oscillation with  $\Delta q_z^{Fe} = 0.033 \text{ \AA}^{-1}$  corresponding to Fe layer. At 187.5 eV, the optical contrast is high between Fe and  $B_4C$  and provides high sensitivity to Fe/ $B_4C$  interface. At this energy, the difference in scattering intensities of porous  $B_4C$  layer and pure  $B_4C$  layer is high and provides an opportunity to probe interface between pure  $B_4C$  layer and porous  $B_4C$  layer. The best fit results suggest the presence of a low-density porous layer of  $B_4C$  (1.3 nm) with porosity of 35% at bottom of  $B_4C$  layer. To distinguish the effect of roughness and porosity on the measured reflectivity profile, we have done simulations taking these two parameters independently. Roughness only reduces the reflectivity but presence of porous interlayer redistributes the soft X-ray reflectivity profile near the absorption edge. The fitted profile with interface roughness (without porosity) deviates significantly from the measured profile. The layer model derived from the best fit is shown in the inset (left side) of Figure 16. At 188.5 eV, the sensitivity of  $B_4C$ /Fe interface decreases due to significant increase in absorption in the  $B_4C$  layer, and oscillations only due to  $B_4C$  layer are observed. The amplitude of intensity modulation is high at large angle due to increased penetration depth. As the energy increases further, for example at 192 eV, the oscillation becomes weak. Thus interface is tuned selectively by adjusting the incident photon energy and the resonant reflectivity profile reveal high sensitivity to specific interface. Utilizing anomalous scattering principle in soft X-ray region, it is possible to selectively probe porous layer of low-Z resonating atom in low-Z thin films.

Using the measured optical constants of  $B_4C$  near the boron K edge, we have analyzed the  $B_4C$ -on-Fe bilayer structure. By fitting the measured reflectivity data of  $B_4C$ -on-Fe bilayer we obtained the thickness depth profile of  $\delta$  (Figure 17). For Fe,  $\delta$  is positive and decreases systematically as the energy increases. For  $B_4C$ , at 185.3 eV,  $\delta \cong 0$  corresponding to  $\delta$  for vacuum. Above 185.3 eV to 188.5 eV,  $\delta$  shows sign reversal. When energy increases above 188.5 eV,  $\delta$  again becomes positive and absorption term,  $\beta$  becomes significant. In  $B_4C$ -on-Fe bilayer, the optical constants of  $B_4C$  vary within  $\sim 2.1\%$  with respect to pure  $B_4C$  thin film. The inset in Figure 17 shows the expanded portion between substrate/Fe and Fe/ $B_4C$  interfaces, marked by vertical line. When we move from  $B_4C$  to porous layer of  $B_4C$ /Fe interface, variation in  $\delta$  is gradual instead of a step function. This is due to small variation of  $\delta$  and low thickness of the porous layer



TABLE 2: SXRR measurements of B<sub>4</sub>C-on-Fe bilayer film.

Energy (eV)	$\delta_{\text{B}_4\text{C}}$ (expt.)	$\beta_{\text{B}_4\text{C}}$ (expt.)	$\delta_{\text{Fe}}$ (expt.)	$\delta_{\text{Fe}}$ (Henke et al.)	$\beta_{\text{Fe}}$ (expt.)	$\delta_{\text{Fe}}$ (Henke et al.)
185.3	0.00001	0.0003	0.0233	0.02349	0.0131	0.01292
187.5	-0.0084	0.0007	0.0227	0.02312	0.0122	0.01256
188.5	-0.0058	0.0084	0.0224	0.02295	0.0121	0.01238
192	0.0015	0.0097	0.0219	0.02234	0.0116	0.01198

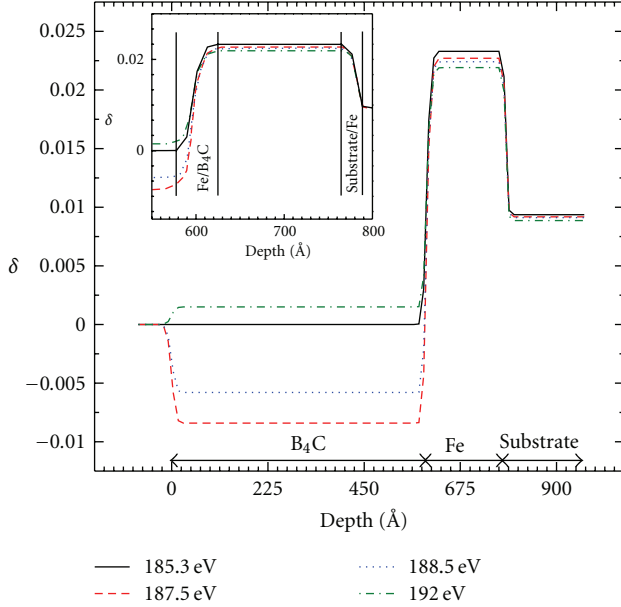
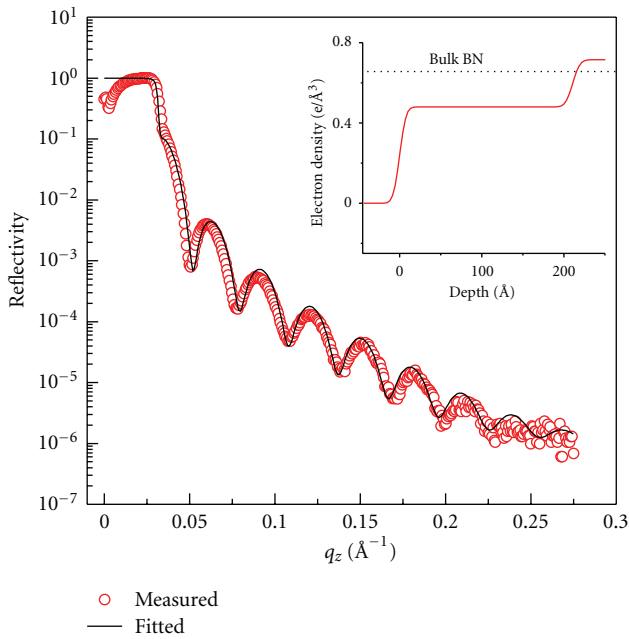
FIGURE 17: Depth variation of dispersion part of refractive index ( $\delta$ ) obtained after fitting of the measured soft XRR profile of Figure 16. The inset shows the Fe/B<sub>4</sub>C and Substrate/Fe interface.

FIGURE 18: XRR spectrum of BN thin film (21.7 nm) at 8047 eV. In the inset, the continuous line shows EDP profile of the thin film and the dotted line shows bulk values.

(1.3 nm). The smoothening is not due to roughness at the Fe/B<sub>4</sub>C interface.

**4.4. Determination of Native Oxide Layer.** Many elements when exposed to ambient have a native oxide on the surface. For improvement of material properties it is important to have reliable knowledge about thickness, roughness and density of the native oxide. The native oxide has low optical contrast and low thickness (usually few nm). The contrast problem is severe in-case of low-Z oxides. Probing of native oxide with high accuracy is a challenging task. The difficulty in probing native oxide (low contrast system) with more accuracy using laboratory-based X-ray reflectometry is due to comparative low dynamical range ( $\sim 10^{-6}$ ). However, using high flux synchrotron radiation where the reflectivity can be measured over  $\sim 8$  to 9 orders, native oxide can be studied more reliably, for example in case of silicon/silicon oxide [110]. Sakurai and Iida [7] used Fourier analysis method of specular X-ray reflectivity to determine thickness of native silicon oxide on silicon. Possibility of probing native oxide using SXRR has not been exploited yet. Here we propose the possibility to determine native oxide using SXRR with high sensitivity. Also SXRR provides additional information regarding possible composition of the oxide layer. We have demonstrated this through characterization of boron oxide on BN thin film using both simulations and measurements near B K-edge. Before SXRR study, the BN thin is characterized using XRR.

The measured XRR profile of BN thin film at 8047 eV along with the fitted profile is shown in Figure 18. The measured reflectivity profile shows interference oscillation with large amplitude modulation, which was not expected in case of BN film deposited on Si substrate because of poor material density contrast. The observed large amplitude modulation reveals the large change in density of deposited BN film compared to the bulk value. The inset shows electron density profile (EDP) of the film (continuous line), obtained from the best fit XRR profile. The dotted line represents bulk electron density for BN. The fitted profile matches with the measured curve, considering a single layer model (without considering oxide). The best fit XRR results reveal, 21 nm BN layer with root mean square (rms) roughness  $\sim 0.6$  nm. The best fit optical constant of BN film is  $\delta = 5.15 \times 10^{-6}$  and  $\beta = 9.8 \times 10^{-9}$ . The roughness of substrate is  $\sim 0.7$  nm. The average electron density of BN layer is  $0.48 \text{ e}/\text{\AA}^3$ , which is  $\sim 73\%$  of the bulk value ( $0.656 \text{ e}/\text{\AA}^3$ ). There is no signature of oxide layer from XRR data analysis.

In ion beam sputtered deposited BN film, there is a possibility of individual B and N. The elementary B when exposed

to ambient will get oxidized. So, there may be possibility of oxide formation at top of BN film. The sensitivity to identify oxide layer was studied through simulations of SXRR profiles before undertaking actual measurements. Figure 19 shows a comparison of the scattering strength,  $\Delta\delta^2 + \Delta\beta^2$ , at different interfaces near B K-edge. Figure 19(a) shows scattering strength at BN with different boron oxide, that is, BN/B<sub>2</sub>O<sub>3</sub>, BN/B<sub>2</sub>O and at interface between B<sub>2</sub>O<sub>3</sub>/B<sub>2</sub>O. Figure 19(b) shows scattering strength of BN, B<sub>2</sub>O<sub>3</sub> and B<sub>2</sub>O with respect to vacuum. Density of BN was taken as 2.25 gm/cm<sup>3</sup>. The density of B<sub>2</sub>O and B<sub>2</sub>O<sub>3</sub> was taken as 2.24 [111] and 1.844 gm/cm<sup>3</sup> [112], respectively. In Figure 19, just near the edge, the scattering strength changes significantly. Particularly a large change in scattering strength is observed at oxide/oxide (with different composition), B<sub>2</sub>O/Vacuum and BN/Vacuum interface. This large change in scattering strength will be sufficient to be model fitting the observed reflectivity profile. Also due to large change in scattering strength between two different oxide compositions, it will also be possible to identify more than one oxide layer in the film. To observe these predictions, we carried out SXRR measurements on BN film by changing incident photon energy near B K-edge.

Figure 20 shows measured SXRR profiles of BN thin film by tuning incident photon in a narrow energy range, near the boron K-edge. The inset shows optical constants of B<sub>2</sub>O<sub>3</sub> (calculated using Henke et al.) and BN (measured) near the edge. The arrows in inset indicate the small energy range over which the measured reflectivity pattern is shown. Within the small energy range (from 187.85 to 188.5 eV), all the reflectivity profiles undergo a large variation. The modulation in the measured reflectivity profile within a small energy range is such that it is difficult to consider this due to change in either roughness or due to presence of porous layer, as seen by simulations. Something else is responsible for the large change in reflectivity pattern. One possibility is due to presence of some chemical changes in films. This may give large variation in scattering strength near the edge which is reflected in the observed reflectivity profile. This chemical change may be due to formation of boron oxide layer on the top surface of the film due to reaction of oxygen with decomposed boron when exposed to ambient. In inset of Figure 20, in the energy range over which SXRR measurements are performed (marked by arrow), the optical constants of calculated B<sub>2</sub>O<sub>3</sub> and measured BN change significantly. This variation in optical constants may be the cause of large modulation in observed reflectivity profile. This provides a starting guess in SXRR curve fitting, to consider presence of oxide layer on the top of the BN film.

Figure 21 shows the same measured reflectivity pattern (as shown in Figure 20) along with fitted curve with different models. For the single layer model, the structural parameters such as thickness, roughness and density, obtained from XRR, are used, and the optical constant ( $\delta$  and  $\beta$ ) are taken from the Henke et al. calculated values as the starting guess. In case of single layer model, even if we allow variation in the film roughness, thickness and optical constant, in the model, the fitted curve is far from the measured profile. The best fit curve using single layer model does not predict the actual

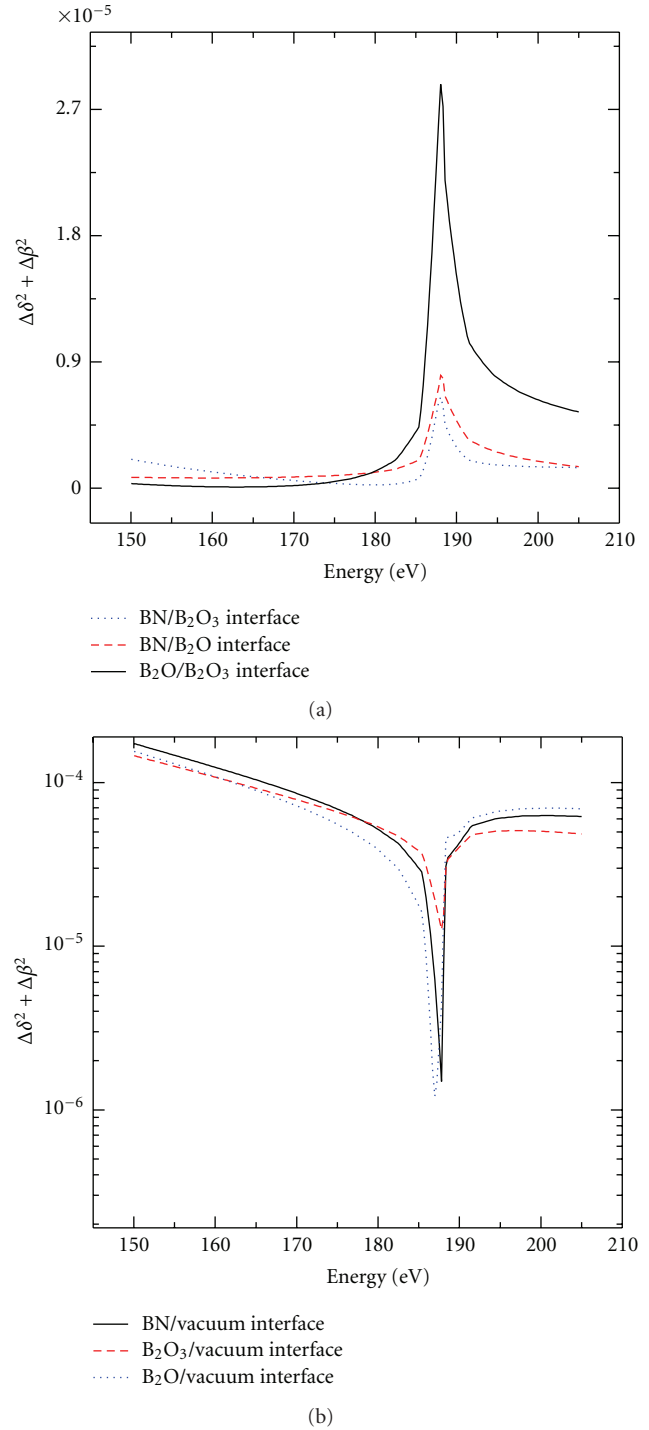


FIGURE 19: Comparison of the scattering strength,  $\Delta\delta^2 + \Delta\beta^2$ , at different interfaces near B K-edge. (a) BN/B<sub>2</sub>O<sub>3</sub>, BN/B<sub>2</sub>O and B<sub>2</sub>O<sub>3</sub>/B<sub>2</sub>O. (b) BN/vacuum, B<sub>2</sub>O<sub>3</sub>/vacuum and B<sub>2</sub>O/vacuum.

structure of the thin film. Using idea from the scattering strength profile, fitting was performed considering different oxide layers. The total thickness of the film, roughness of the film and substrate as obtained by XRR are kept fixed during SXRR profile simulation. Optical constants of the substrate are kept constant as per Henke et al. database. In

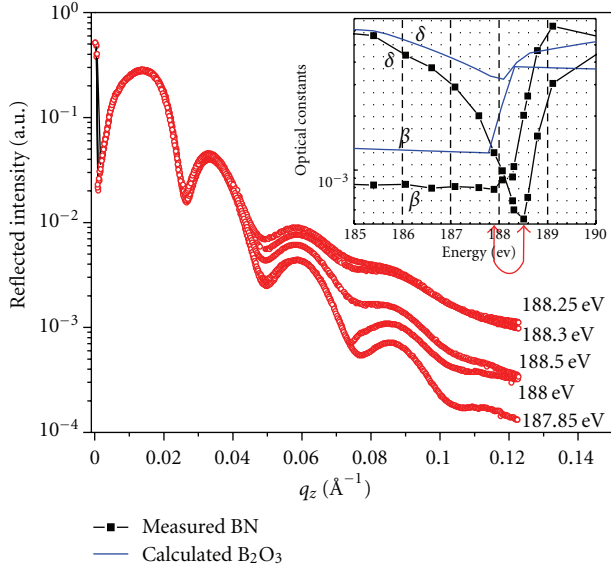


FIGURE 20: Measured SXRR profiles of BN thin film at selected energies near boron K-edge. The inset shows optical constants of  $B_2O_3$  (calculated) and BN (measured) near edge to compare the effect of optical constants on reflectivity pattern. The arrows in inset indicate the small energy range over which the measured reflectivity pattern shown.

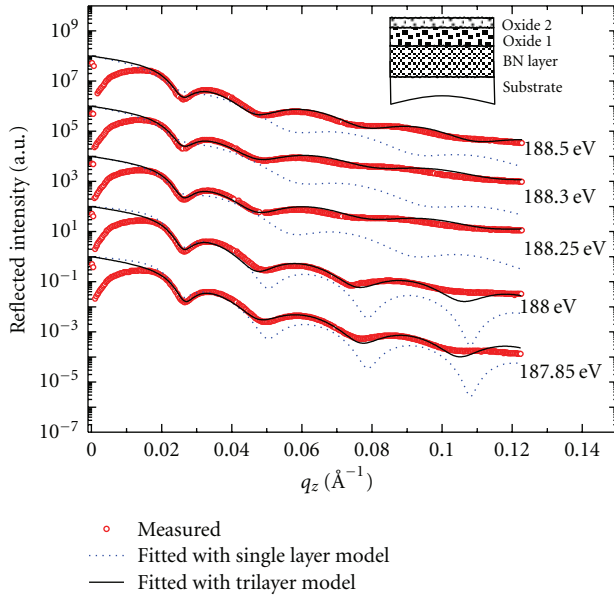


FIGURE 21: Measured SXRR profiles of BN thin film (21 nm) near boron K-edge is fitted with different model. The best fit is obtained for trilayer model. The inset shows the best fit model.

oxide layer model, thicknesses of different layers are varied keeping total film thickness constant as per XRR value. Starting guess for optical constant of different layers are taken from Henke et al. calculated database. The best fit curve is very close to the measured profile with trilayer model (inset of Figure 21). The bottom most layer is BN layer without oxide, the other two layers are boron oxide with

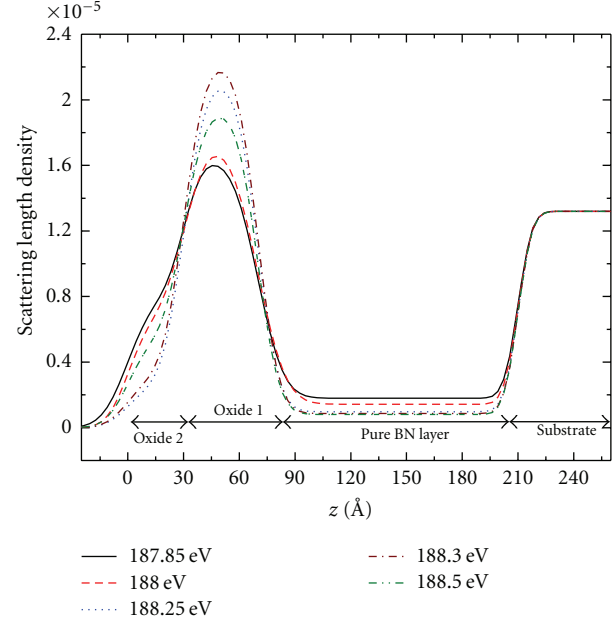


FIGURE 22: Scattering length density profile derived from best fit results using trilayer model for BN thin films near B K-edge.

different composition. The present case is complex, because in BN layer there may also dissociated B and N. Similarly, in boron oxide there may be presence of BN compound. The fitted curve can be further improved by considering proper combinations in all the layers. As per the present best fit curve, the thickness of BN, oxide 1 and oxide 2 are  $\sim 14$ , 4 and 3 nm, respectively. The optical constants of BN layer obtained from best fit data are given in inset of Figure 20 (also see in Figure 4). The scattering length density profile obtained from the best fit data using trilayer model is shown in Figures 21 and 22. At these energies, scattering length density of three different layers are significantly different, and undergoes large variation within these small energy range, especially for oxide 1. The oxide layer 2, which has slightly higher scattering length density with respect to BN, may be presence of oxygen rich boron oxide along with BN. The oxide layer 1, is attributed to boron rich boron oxide along with BN. More details about the chemical nature of oxygen and nitrogen could also be obtained by performing SXRR measurements near oxygen and nitrogen K absorption edge. Again, the analysis will be simple if a layer consists of single composition instead of mixture of composition. The presence of oxide in the present sample has been confirmed using X-ray photo electron spectroscopy. The more detailed study by correlating with photoelectron spectroscopy will be presented elsewhere. The present observation conform, SXRR will be a powerful nondestructive analytical tool for probing native oxide with high sensitivity. SXRR is also sensitive to variation in atomic composition of oxide.

## 5. Conclusion

We provide an overview of the possibility of structural study of hard condensed matter thin films containing resonating

low-Z element by exploiting tunable and enhanced resonant scattering contrast in the soft X-ray region through resonant reflectivity technique. We used layer and elemental-specificity properties of resonant reflectivity as complementary technique with layer specificity of conventional hard X-ray reflectivity for these applications. Soft X-ray resonant reflectivity is sensitive to atomic composition and density variation in thin films. The unique utility of soft X-ray resonant reflectivity for low-Z elements is discussed through number of representative applications such as determination of interlayer composition at buried interface, probing depth profiling of atomic density and sensitivity to native oxide and composition with nearly equal electron density. Soft X-ray resonant reflectivity can be a powerful nondestructive technique to analyze detail structural parameters with high sensitive in thin film and multilayer structures containing resonating low-Z atoms with poor electron density contrast.

## Acknowledgments

The authors gratefully acknowledge S. K. Deb for encouragement for this work. The authors also sincerely acknowledge late T. T. Prasad with deep gratitude for his constant support during sample fabrication using electron beam evaporation system. The authors also sincerely acknowledge A. K. Sinha, P. N. Rao, M. H. Modi, and S. Rai for their help in doing X-ray reflectivity measurements. The authors also thank R. Dhawan for help in sample preparation using ion beam sputtering.

## References

- [1] L. G. Parratt, "Surface studies of solids by total reflection of X-rays," *Physical Review*, vol. 95, no. 2, pp. 359–369, 1954.
- [2] S. K. Ghose and B. N. Dev, "X-ray standing wave and reflectometric characterization of multilayer structures," *Physical Review B*, vol. 63, no. 24, Article ID 245409, 11 pages, 2001.
- [3] S. K. Ghose, D. K. Goswami, B. Rout, B. N. Dev, G. Kuri, and G. Materlik, "Ion-irradiation-induced mixing, interface broadening and period dilation in Pt/C multilayers," *Applied Physics Letters*, vol. 79, no. 4, pp. 467–469, 2001.
- [4] T. V. Chandrasekhar Rao and M. K. Sanyal, "The effect of growth defects on the X-ray reflectivity of multilayer systems," *Applied Surface Science*, vol. 74, no. 4, pp. 315–321, 1994.
- [5] M. K. Sanyal, J. K. Basu, A. Datta, and S. Banerjee, "Determination of small fluctuations in electron density profiles of thin films: layer formation in a polystyrene film," *Europhysics Letters*, vol. 36, no. 4, pp. 265–270, 1996.
- [6] S. K. Sinha, E. B. Sirota, S. Garoff, and H. B. Stanley, "X-ray and neutron scattering from rough surfaces," *Physical Review B*, vol. 38, no. 4, pp. 2297–2311, 1988.
- [7] K. Sakurai and A. Iida, "Fourier analysis of interference structure in X-ray specular reflection from thin films," *Japanese Journal of Applied Physics*, vol. 31, no. 2A, pp. L113–L115, 1992.
- [8] G. Vignaud, A. Gibaud, G. Grübel et al., "Ordering of diblock PS-PBMA thin films: an X-ray reflectivity study," *Physica B*, vol. 248, no. 1–4, pp. 250–257, 1998.
- [9] C. J. Yu, A. G. Richter, A. Datta, M. K. Durbin, and P. Dutta, "Observation of molecular layering in thin liquid films using X-ray reflectivity," *Physical Review Letters*, vol. 82, no. 11, pp. 2326–2329, 1999.
- [10] O. H. Seeck, I. D. Kaendler, M. Tolan et al., "Analysis of X-ray reflectivity data from low-contrast polymer bilayer systems using a Fourier method," *Applied Physics Letters*, vol. 76, no. 19, pp. 2713–2715, 2000.
- [11] G. Evmenenko, S. W. Dugan, J. Kmetko, and P. Dutta, "Molecular ordering in thin liquid films of polydimethylsiloxanes," *Langmuir*, vol. 17, no. 13, pp. 4021–4024, 2001.
- [12] T. Koga, Y. S. Seo, J. L. Jerome et al., "Low-density polymer thin film formation in supercritical carbon dioxide," *Applied Physics Letters*, vol. 83, no. 21, pp. 4309–4311, 2003.
- [13] L. Grave de Peralta and H. Temkin, "Improved Fourier method of thickness determination by X-ray reflectivity," *Journal of Applied Physics*, vol. 93, no. 4, pp. 1974–1977, 2003.
- [14] B. Bataillou, H. Moriceau, and F. Rieutord, "Direct inversion of interfacial reflectivity data using the Patterson function," *Journal of Applied Crystallography*, vol. 36, no. 6, pp. 1352–1355, 2003.
- [15] F. Bridou, J. Gautier, F. Delmotte, M. F. Ravet, O. Durand, and M. Modreanu, "Thin multilayers characterization by grazing X-ray reflectometry and use of Fourier transform," *Applied Surface Science*, vol. 253, no. 1, pp. 12–16, 2006.
- [16] K. Sakurai, M. Mizusawa, and M. Ishii, "Significance of frequency analysis in X-ray reflectivity: towards analysis which does not depend too much on models," *Transactions of the Materials Research Society of Japan*, vol. 33, no. 3, pp. 523–528, 2008.
- [17] O. G. Shpyrko, A. Yu. Grigoriev, R. Streitel et al., "Atomic-scale surface demixing in a eutectic liquid BiSn alloy," *Physical Review Letters*, vol. 95, no. 10, Article ID 106103, 4 pages, 2005.
- [18] D. R. Lee, S. K. Sinha, D. Haskel et al., "X-ray resonant magnetic scattering from structurally and magnetically rough interfaces in multilayered systems. I. Specular reflectivity," *Physical Review B*, vol. 68, no. 22, Article ID 224409, 19 pages, 2003.
- [19] C. Vettier, "Resonant X-ray scattering in transition metal and rare-earth materials," *Journal of Electron Spectroscopy and Related Phenomena*, vol. 117–118, pp. 113–128, 2001.
- [20] Y. S. Chu, H. You, J. A. Tanzer, T. E. Lister, and Z. Nagy, "Surface resonance X-ray scattering observation of core-electron binding-energy shifts of Pt(111)-surface atoms during electrochemical oxidation," *Physical Review Letters*, vol. 83, no. 3, pp. 552–555, 1999.
- [21] G. Materlik, C. J. Sparks, and K. Fischer, Eds., *Resonant Anomalous X-Ray Scattering: Theory and Applications*, North-Holland, Amsterdam, The Netherlands, 1994.
- [22] H. Ade, X. Zhang, S. Cameron, C. Costello, J. Kirz, and S. Williams, "Chemical contrast in X-ray microscopy and spatially resolved XANES spectroscopy of organic specimens," *Science*, vol. 258, no. 5084, pp. 972–975, 1992.
- [23] D. Vaknin, P. Krüger, and M. Lösche, "Anomalous X-ray reflectivity characterization of ion distribution at biomimetic membranes," *Physical Review Letters*, vol. 90, no. 17, Article ID 178102, 4 pages, 2003.
- [24] C. Park, P. A. Fenter, N. C. Sturchio, and J. R. Regalbuto, "Probing out-sphere adsorption of aqueous metal complexes at the oxide-water interface with resonant anomalous X-ray reflectivity," *Physical Review Letters*, vol. 94, no. 7, Article ID 076104, 4 pages, 2005.
- [25] D. H. Kim, H. H. Lee, S. S. Kim et al., "Chemical depth profile of passive oxide on stainless steel," *Applied Physics Letters*, vol. 85, no. 26, pp. 6427–6429, 2004.



- [26] K. S. Lee, S. K. Kim, and J. B. Kortright, "Atomic-scale depth selectivity of soft X-ray resonant Kerr effect," *Applied Physics Letters*, vol. 83, no. 18, pp. 3764–3766, 2003.
- [27] J. Strzalka, E. Dimasi, I. Kuzmenko, T. Gog, and J. K. Blasie, "Resonant X-ray reflectivity from a bromine-labeled fatty acid Langmuir monolayer," *Physical Review E*, vol. 70, no. 5, Article ID 051603, 5 pages, 2004.
- [28] W. Bu, P. J. Ryan, and D. Vaknin, "Ion distributions at charged aqueous surfaces by near-resonance X-ray spectroscopy," *Journal of Synchrotron Radiation*, vol. 13, no. 6, pp. 459–463, 2006.
- [29] S. Banerjee, Y. J. Park, D. R. Lee et al., "Anomalous X-ray reflectivity study of metal oxide thin films," *Applied Surface Science*, vol. 136, no. 1–2, pp. 41–45, 1998.
- [30] M. K. Sanyal, S. K. Sinha, A. Gibaud et al., "Fourier reconstruction of density profiles of thin films using anomalous X-ray reflectivity," *Europhysics Letter*, vol. 21, no. 6, pp. 691–696, 1993.
- [31] T. Ohkawa, Y. Yamaguchi, O. Sakata et al., "Anomalous dispersion X-ray reflectometry for model-independent determination of Al/C multilayer structures," *Physica B*, vol. 221, no. 1–4, pp. 416–419, 1996.
- [32] C. Park and P. A. Fenter, "Phasing of resonant anomalous X-ray reflectivity spectra and direct Fourier synthesis of element-specific partial structures at buried interfaces," *Journal of Applied Crystallography*, vol. 40, no. 2, pp. 290–301, 2007.
- [33] M. Feygenson, E. Kentzinger, N. Ziegenhagen et al., "Contrast variation by anomalous X-ray scattering applied to investigation of the interface morphology in a giant magnetoresistance Fe/Cr/Fe trilayer," *Journal of Applied Crystallography*, vol. 40, no. 3, pp. 532–538, 2007.
- [34] H. Stragier, J. O. Cross, J. J. Rehr, L. B. Sorensen, C. E. Bouldin, and J. C. Woicik, "Diffraction anomalous fine structure: a new X-ray structural technique," *Physical Review Letters*, vol. 69, no. 21, pp. 3064–3067, 1992.
- [35] A. Létoublon, V. Favre-Nicolin, H. Renevier et al., "Strain, size, and composition of InAs quantum sticks embedded in InP determined via grazing incidence X-ray anomalous diffraction," *Physical Review Letters*, vol. 92, no. 18, Article ID 186101, 4 pages, 2004.
- [36] G. M. Luo, Z. H. Mai, T. P. A. Hase et al., "Variable wavelength grazing incidence X-ray reflectivity measurements of structural changes on annealing Cu/NiFe multilayers," *Physical Review B*, vol. 64, no. 24, Article ID 245404, 7 pages, 2001.
- [37] C. Wang, T. Araki, and H. Ade, "Soft X-ray resonant reflectivity of low-Z materials thin films," *Applied Physics Letters*, vol. 87, no. 21, Article ID 214109, 3 pages, 2005.
- [38] G. E. Mitchell, B. G. Landes, J. Lyons et al., "Molecular bond selective X-ray scattering for nanoscale analysis of soft matter," *Applied Physics Letters*, vol. 89, no. 4, Article ID 044101, 3 pages, 2006.
- [39] C. Wang, T. Araki, B. Watts et al., "Resonant soft X-ray reflectivity of organic thin films," *Journal of Vacuum Science & Technology A*, vol. 25, no. 3, pp. 575–586, 2007.
- [40] J. M. Virgili, Y. Tao, J. B. Kortright, N. P. Balsara, and R. A. Segalman, "Analysis of order formation in block copolymer thin films using resonant soft X-ray scattering," *Macromolecules*, vol. 40, no. 6, pp. 2092–2099, 2007.
- [41] H. Ade and A. P. Hitchcock, "NEXAFS microscopy and resonant scattering: composition and orientation probed in real and reciprocal space," *Polymer*, vol. 49, no. 3, pp. 643–675, 2008.
- [42] C. Wang, A. Garcia, H. Yan et al., "Interfacial widths of conjugated polymer bilayers," *Journal of the American Chemical Society*, vol. 131, no. 35, pp. 12538–12539, 2009.
- [43] H. Ade, C. Wang, A. Garcia et al., "Characterization of multicomponent polymer trilayers with resonant soft X-ray reflectivity," *Journal of Polymer Science, Part B*, vol. 47, no. 13, pp. 1291–1299, 2009.
- [44] S. Swaraj, C. Wang, T. Araki et al., "The utility of resonant soft X-ray scattering and reflectivity for the nanoscale characterization of polymers," *European Physical Journal: Special Topics*, vol. 167, no. 1, pp. 121–126, 2009.
- [45] J. Daillant, "Recent developments and applications of grazing incidence scattering," *Current Opinion in Colloid and Interface Science*, vol. 14, no. 6, pp. 396–401, 2009.
- [46] S. Swaraj, C. Wang, H. Yan et al., "Nanomorphology of bulk heterojunction photovoltaic thin films probed with resonant soft X-ray scattering," *Nano Letters*, vol. 10, no. 8, pp. 2863–2869, 2010.
- [47] S. Stuhmann, M. Marmotti, H. B. Stuhmann, J. Thomas, C. Trame, and M. S. Lehmann, "Techniques of anomalous X-ray scattering from low-Z elements," *Nuclear Instruments and Methods in Physics Research, Section B*, vol. 133, no. 1–4, pp. 151–156, 1997.
- [48] H. Hogrefe and C. Kunz, "Soft X-ray scattering from rough surfaces: experimental and theoretical analysis," *Applied Optics*, vol. 26, no. 14, pp. 2851–2859, 1987.
- [49] J. A. Carlisle, L. J. Terminello, E. A. Hudson et al., "Characterization of buried thin films with resonant soft X-ray fluorescence," *Applied Physics Letters*, vol. 67, no. 1, pp. 34–36, 1995.
- [50] M. Adamczyk, S. Eisebitt, A. Karl et al., "Surface roughness and resonant scattering effects in soft X-ray speckle from random semiconductor interfaces," *Surface Review and Letters*, vol. 6, no. 6, pp. 1121–1128, 1999.
- [51] P. D. Hatten, S. B. Wilkins, T. A. W. Beale, T. K. Johal, D. Prabhakaran, and A. T. Boothroyd, "Resonant soft X-ray diffraction-In extremis," *Journal of Synchrotron Radiation*, vol. 12, no. 4, pp. 434–441, 2005.
- [52] S. P. Singh, M. H. Modi, and P. Srivastava, "Growth kinetics and compositional analysis of silicon rich a-SiN<sub>x</sub>:H film: a soft X-ray reflectivity study," *Applied Physics Letters*, vol. 97, no. 15, Article ID 151906, 3 pages, 2010.
- [53] H. Wadati, D. G. Hawthorn, J. Geck et al., "Resonant soft X-ray scattering studies of interface reconstructions in SrTiO<sub>3</sub>/LaAlO<sub>3</sub> superlattices," *Journal of Applied Physics*, vol. 106, no. 8, Article ID 083705, 5 pages, 2009.
- [54] M. Nayak, G. S. Lodha, A. K. Sinha, R. V. Nandedkar, and S. A. Shivashankar, "Determination of interlayer composition at buried interfaces using soft X-ray resonant reflectivity," *Applied Physics Letters*, vol. 89, no. 18, Article ID 181920, 3 pages, 2006.
- [55] M. Nayak, G. S. Lodha, T. T. Prasad, P. Nageswararao, and A. K. Sinha, "Probing porosity at buried interfaces using soft X-ray resonant reflectivity," *Journal of Applied Physics*, vol. 107, no. 2, Article ID 023529, 5 pages, 2010.
- [56] R. Loudon, *The Quantum Theory of Light*, Oxford University Press, London, UK, 2nd edition, 1983.
- [57] J. D. Jackson, *Classical Electrodynamics*, Wiley, New York, NY, USA, 3rd edition, 1998.
- [58] D. Attwood, *Soft X-Rays and Extreme Ultraviolet Radiation*, Cambridge University Press, Cambridge, UK, 1999.
- [59] D. Y. Smith and J. H. Barkyoumb, "Sign reversal of the atomic scattering factor and grazing-incidence transmission at

- X-ray-absorption edges," *Physical Review B*, vol. 41, no. 16, pp. 11529–11535, 1990.
- [60] M. Benfatto and R. Felici, "Resonant atomic scattering factor theory: a multiple scattering approach," *Physical Review B*, vol. 64, no. 11, Article ID 115410, 9 pages, 2001.
- [61] B. L. Henke, E. M. Gullikson, and J. C. Davis, "X-ray interactions: photoabsorption, scattering, transmission, and reflection at  $E = 50\text{--}30,000$  eV,  $Z = 1\text{--}92$ ," *Atomic Data and Nuclear Data Tables*, vol. 54, no. 2, pp. 181–342, 1993.
- [62] J. A. Nielsen and D. McMorrow, *Elements of Modern X-Ray Physics*, John Wiley & Sons, New York, NY, USA, 2001.
- [63] E. Spiller, *Soft X-Ray Optics*, SPIE Optical Engineering Press, Washington, DC, USA, 1994.
- [64] E. Filatova, V. Lukyanov, R. Barchewitz, J. M. André, M. Idir, and P. Stemmler, "Optical constants of amorphous  $\text{SiO}_2$  for photons in the range of 60–3000 eV," *Journal of Physics. Condensed Matter*, vol. 11, no. 16, pp. 3355–3370, 1999.
- [65] T. W. Barbee Jr., W. K. Warburton, and J. H. Underwood, "Determination of the X-ray anomalous dispersion of titanium made with a titanium-carbon layered synthetic microstructure," *Journal of the Optical Society of America B*, vol. 1, no. 5, pp. 691–698, 1984.
- [66] R. Soufli and E. M. Gullikson, "Reflectance measurements on clean surfaces for the determination of optical constants of silicon in the extreme ultraviolet-soft-X-ray region," *Applied Optics*, vol. 36, no. 22, pp. 5499–5507, 1997.
- [67] P. Tripathi, G. S. Lodha, M. H. Modi, A. K. Sinha, K. J. S. Sawhney, and R. V. Nandedkar, "Optical constants of silicon and silicon dioxide using soft X-ray reflectance measurements," *Optics Communications*, vol. 211, no. 1–6, pp. 215–223, 2002.
- [68] M. Magnuson and C. F. Hague, "Determination of the refractive index at soft X-ray resonances," *Journal of Electron Spectroscopy and Related Phenomena*, vol. 137–140, pp. 519–522, 2004.
- [69] L. Sève, J. M. Tonnerre, and D. Raoux, "Determination of the anomalous scattering factors in the soft X-ray range using diffraction from a multilayer," *Journal of Applied Crystallography*, vol. 31, no. 5, pp. 700–707, 1998.
- [70] D. Ksenzov, C. Schlemper, and U. Pietsch, "Resonant soft X-ray reflectivity of  $\text{Me/B}_4\text{C}$  multilayers near the boron K edge," *Applied Optics*, vol. 49, no. 25, pp. 4767–4773, 2010.
- [71] D. E. Aspnes, "The accurate determination of optical properties by Ellipsometry," in *Handbook of Optical Constants of Solids*, E. D. Palik, Ed., pp. 89–112, Academic Press, London, UK, 1998.
- [72] R. Mancke, "Optical properties of molybdenum by electron energy loss spectroscopy," *Physica Status Solidi (B)*, vol. 97, no. 1, pp. 157–160, 1980.
- [73] D. P. Siddons, "Some applications of X-ray interferometry," in *AIP Proceedings of the Topical Conference on Low Energy X-Ray Diagnostics*, D. T. Attwood and B. L. Menke, Eds., vol. 75, pp. 236–241, AIP, New York, NY, USA, 1981.
- [74] L. T. Lee, D. Langevin, E. K. Mann, and B. Farnoux, "Neutron reflectivity at liquid interfaces," *Physica B*, vol. 198, no. 1–3, pp. 83–88, 1994.
- [75] J. Strzalka, B. R. Gibney, S. Satija, and J. K. Blasie, "Specular neutron reflectivity and the structure of artificial protein maquettes vectorially oriented at interfaces," *Physical Review E*, vol. 70, no. 6, Article ID 061905, 10 pages, 2004.
- [76] A. G. Michette, "X-ray microscopy," *Reports on Progress in Physics*, vol. 51, no. 12, pp. 1525–1606, 1988.
- [77] J. Kirz, C. Jacobsen, and M. Howells, "Soft X-ray microscopes and their biological applications," *Quarterly Reviews of Biophysics*, vol. 28, no. 1, pp. 33–130, 1995.
- [78] M. Born and E. Wolf, *Principles of Optics*, Pergamon, New York, NY, USA, 1980.
- [79] L. V. Azaroff, R. Kaplow, N. Kato, R. J. Weiss, A. J. C. Wilson, and R. A. Young, *X-Ray Diffraction*, McGraw-Hill, New York, NY, USA, 1974.
- [80] F. Abeles, "Recherches sur la propagation des ondes électromagnétiques sinusoidales dans les milieux stratifiés," *Annales de Physique*, vol. 5, p. 596, 1950.
- [81] E. Ziegler, "Multilayers for high heat load synchrotron applications," *Optical Engineering*, vol. 34, no. 2, pp. 445–452, 1995.
- [82] H. Kiessig, "Interferenz von Röntgenstrahlen an dünnen Schichten," *Annalen Der Physik*, vol. 402, no. 7, pp. 769–788, 1931.
- [83] J. M. Cowley, *Diffraction Physics*, North-Holland, Amsterdam, The Netherlands, 1975.
- [84] V. Holy, U. Pietsch, and T. Baumbach, *High-Resolution X-Ray Scattering from Thin Films and Multilayers*, Springer, Berlin, Germany, 1999.
- [85] C. Giacobozzo, H. L. Monaco, and S. D. Viterbo, *Fundamentals of Crystallography*, Oxford Science Publications, Oxford, UK, 1991.
- [86] L. Nevot and P. Croce, "Caractérisation des surfaces par réflexion rasante de rayons X. Application à l'étude du polissage de quelques verres silicates," *Revue Physics Applied*, vol. 15, pp. 761–779, 1980.
- [87] M. Tolan, *X-Ray Scattering from Soft-Matter Thin Films*, Springer, Berlin, Germany, 1999.
- [88] V. Holý and T. Baumbach, "Nonspecular X-ray reflection from rough multilayers," *Physical Review B*, vol. 49, no. 15, pp. 10668–10676, 1994.
- [89] M. Nayak, B. Gowrisankar, A. Verma, and G. S. Lodha, "Electron beam evaporation system for depositing X-ray multilayer mirrors," *Asian Journal of Physics*, vol. 16, no. 4, pp. 395–405, 2007.
- [90] S. Rai, M. K. Tiwari, G. S. Lodha et al., "Surface and interface study of pulsed-laser-deposited off-stoichiometric  $\text{NiMnSb}$  thin films on a  $\text{Si}(100)$  substrate," *Physical Review B*, vol. 73, no. 3, Article ID 035417, 5 pages, 2006.
- [91] R. V. Nandedkar, K. J. S. Sawhney, G. S. Lodha et al., "First results on the reflectometry beamline on Indus-1," *Current Science*, vol. 82, no. 3, pp. 298–304, 2002.
- [92] R. Soufli and E. M. Gullikson, "Optical constants of materials for multilayer mirror applications in the EUV/soft X-ray region," in *Grazing Incidence and Multilayer X-Ray Optical Systems*, R. B. Hoover and A. B. C. Walker II, Eds., vol. 3113 of *Proceedings of SPIE*, pp. 222–229, San Diego, Calif, USA, 1997.
- [93] K. D. Joensen, P. Gorenstein, F. E. Christensen, G. Guttmann, and J. L. Wood, "Grazing incidence Fe-line telescopes using  $\text{W/B}_4\text{C}$  multilayers," *Optical Engineering*, vol. 34, no. 1, pp. 283–288, 1995.
- [94] A. Kazimirov, D. M. Smilgies, Q. Shen et al., "Multilayer X-ray optics at CHESS," *Journal of Synchrotron Radiation*, vol. 13, no. 2, pp. 204–210, 2006.
- [95] T. W. Barbee Jr., S. Mrowka, and M. C. Hettrick, "Molybdenum-silicon multilayer mirrors for the extreme ultraviolet," *Applied Optics*, vol. 24, no. 6, pp. 883–886, 1985.
- [96] D. L. Windt and W. K. Waskiewicz, "Multilayer facilities required for extreme-ultraviolet lithography," *Journal of*

- Vacuum Science and Technology B*, vol. 12, no. 6, pp. 3826–3832, 1994.
- [97] M. Toyoda, Y. Shitani, M. Yanagihara, T. Ejima, M. Yamamoto, and M. Watanabe, “A soft-X-ray imaging microscope with a multilayer-coated schwarzschild objective: imaging tests,” *Japanese Journal of Applied Physics, Part 1*, vol. 39, no. 4A, pp. 1926–1929, 2000.
  - [98] R. Soufli, A. L. Aquila, F. Salmassi, M. Fernández-Perea, and E. M. Gullikson, “Optical constants of magnetron-sputtered boron carbide thin films from photoabsorption data in the range 30 to 770 eV,” *Applied Optics*, vol. 47, no. 25, pp. 4633–4639, 2008.
  - [99] D. Ksenzov, T. Panzner, C. Schlemper, C. Morawe, and U. Pietsch, “Optical properties of boron carbide near the boron K edge evaluated by soft-X-ray reflectometry from a Ru/B<sub>4</sub>C multilayer,” *Applied Optics*, vol. 48, no. 35, pp. 6684–6691, 2009.
  - [100] M. Fernandez-Perea, J. I. Larruquert, J. A. Aznarez et al., “Optical constants of electron-beam evaporated boron films in the 6.8–900 eV photon energy range,” *Journal of Optical Society of America A*, vol. 24, no. 12, pp. 3800–3807, 2007.
  - [101] D. M. Hoffman, G. L. Doll, and P. C. Eklund, “Optical properties of pyrolytic boron nitride in the energy range 0.05–10 eV,” *Physical Review B*, vol. 30, no. 10, pp. 6051–6056, 1984.
  - [102] N. Miyata, K. Moriki, O. Mishima, M. Fujisawa, and T. Hattori, “Optical constants of cubic boron nitride,” *Physical Review B*, vol. 40, no. 17, pp. 12028–12029, 1989.
  - [103] M. Khelkhal and F. Herlemont, “Infrared optical constants of polycrystalline boron nitride,” *Applied Optics*, vol. 32, no. 1, pp. 57–59, 1993.
  - [104] S. Yixi, J. Xin, W. Kun et al., “Vacuum-ultraviolet reflectance spectra and optical properties of nanoscale wurtzite boron nitride,” *Physical Review B*, vol. 50, no. 24, pp. 18637–18639, 1994.
  - [105] S. P. Murarka, *Silicides for VLSI Applications*, Academic Press, London, UK, 1983.
  - [106] J. M. Slaughter, A. Shapiro, P. A. Kearney, and C. M. Falco, “Growth of molybdenum on silicon: structure and interface formation,” *Physical Review B*, vol. 44, no. 8, pp. 3854–3863, 1991.
  - [107] S. Yulin, T. Feigl, T. Kuhlmann et al., “Interlayer transition zones in Mo/Si superlattices,” *Journal of Applied Physics*, vol. 92, no. 3, pp. 1216–1220, 2002.
  - [108] E. A. Brandes and G. B. Brook, Eds., *Smithells Metals Reference Book*, Butterworth-Heinemann, Oxford, UK, 1992.
  - [109] M. Nayak, G. S. Lodha, R. V. Nandedkar, S. M. Chaudhari, and P. Bhatt, “Interlayer composition in Mo-Si multilayers using X-ray photoelectron spectroscopy,” *Journal of Electron Spectroscopy and Related Phenomena*, vol. 152, no. 3, pp. 115–120, 2006.
  - [110] I. M. Tidswell, B. M. Ocko, P. S. Pershan, S. R. Wasserman, G. M. Whitesides, and J. D. Axe, “X-ray specular reflection studies of silicon coated by organic monolayers (alkylsiloxanes),” *Physical Review B*, vol. 41, no. 2, pp. 1111–1128, 1990.
  - [111] H. T. Hall and L. A. Compton, “Group IV analogs and high pressure, high temperature synthesis of B<sub>2</sub>O<sub>3</sub>,” *Inorganic Chemistry*, vol. 4, no. 8, pp. 1213–1216, 1965.
  - [112] A. P. Babichev, “Density of matter,” in *Handbook of Physical Quantities*, I. S. Grigoriev and E. Z. Meilikhov, Eds., chapter 5, pp. 115–144, CRC Press, New York, NY, USA, 1997.



